Many-Objective Optimized Current Reference Generation Strategy for Inverter-Based Distributed Generators During Unbalanced Voltage Sags

Fankai Wen, *Graduate Student Member, IEEE*, Pablo Acuna, *Member, IEEE*, Zhige Yuan, Chenggang Cui, *Member, IEEE*, Ricardo P. Aguilera, *Member, IEEE*, and Amer M. Y. M. Ghias, *Senior Member, IEEE*

***Abstract*—Traditional current reference generators (CRGs) used in low-voltage ride-through (LVRT) control schemes often optimize a single objective, such as minimizing power oscillations, at the expense of other performance metrics such as total harmonic distortion (THD). This article proposes a many-objective optimized current reference generation strategy (MaO-OCRGS) that yields a set of tradeoff solutions, each defined by proposing two decision variables and their associated power quality performance metrics, i.e., power oscillations (Δp, Δq), THD, and the *unbalance index* (UI). A hybrid physics-based and data-driven (HPD) approach is proposed to construct the performance objective functions of a many-objective optimization (MaOO) problem, where the power oscillations are theoretically derived, and an artificial neural network (ANN) is proposed to model the relationships between the decision variables and current-related metrics (THD and UI). A nondominated sorting genetic algorithm III (NSGA-III) is employed to solve the MaOO problem, yielding a set of optimal decision variables. A subsequent postoptimization selection then identifies feasible solutions that prioritize one performance metric while keeping the others within acceptable limits, thereby avoiding undesirable tradeoffs and resulting in three optimized CRGs. Experimental validation demonstrates that the optimized CRGs achieved through the proposed MaO-OCRGS effectively enhance one performance objective without unacceptable degradation in others, as the other metrics are maintained within their predefined limits, thus offering flexibility while enhancing the overall LVRT performance under unbalanced voltage conditions.**

***Index Terms*—Artificial neural network (ANN), current reference generators (CRGs), distributed generations (DGs), grid-connected inverter, low-voltage ride-through (LVRT), NSGA-III, voltage sags.**

Received 23 April 2025; revised 10 July 2025, 17 August 2025, and 9 October 2025; accepted 16 November 2025. Date of publication 24 November 2025; date of current version 25 February 2026. This work was supported in part by Agencia Nacional de Investigacion y Desarrollo (ANID): ANID/FONDECYT Regular/1231265, in part by the Australian Government, Australian Research Council through the Discovery Project under Grant DP240102646, and in part by the School of Electrical and Electronic Engineering, Nanyang Technological University. Recommended for publication by Associate Editor L. Peng. *(Corresponding author: Pablo Acuna; Amer M. Y. M. Ghias.)*

Fankai Wen is with Energy Research Institute at NTU, Interdisciplinary Graduate Programme, Nanyang Technological University, Singapore 639798 (e-mail: fankai001@e.ntu.edu.sg).

Pablo Acuna is with Facultad de Ingenieria, Universidad de Talca, Curico 1145, Chile (e-mail: pablo.acuna@utalca.cl).

Zhige Yuan and Amer M. Y. M. Ghias are with the School of Electrical and Electronic Engineering, Nanyang Technological University, Singapore 639798 (e-mail: zhige002@e.ntu.edu.sg; amer.ghias@ntu.edu.sg).

Chenggang Cui is with the School of Automation, Shanghai University of Electric Power, Shanghai 200090, China (e-mail: cgcui@shiep.edu.cn).

Ricardo P. Aguilera is with the School of Electrical and Data Engineering, University of Technology Sydney, Broadway, NSW 2007, Australia (e-mail: ricardo.aguilera@uts.edu.au).

Color versions of one or more figures in this article are available at https://doi.org/10.1109/TPEL.2025.3635875.

Digital Object Identifier 10.1109/TPEL.2025.3635875

I. Introduction

IN RECENT years, the global adoption and implementation of distributed generation (DG) systems have surged. This paradigm shift in power generation and distribution has gained momentum due to various factors, including advancements in renewable energy technologies, evolving consumer preferences, and the need for a more resilient and sustainable energy infrastructure [1], [2], [3], [4], [5]. However, the widespread integration of DG introduces significant challenges to the continuity of power system service, particularly during disturbances. One of the most critical disturbances is the voltage sag. The growth of DG systems, particularly in the form of renewable energy sources, increases variability and uncertainty in power system operation, which can exacerbate voltage sags due to the intermittent nature of DG output [6], [7]. Additionally, the decentralized deployment of DG often alters power flow patterns and system impedance, making the grid more susceptible to voltage sags during faults or sudden load changes [8].

When the grid experiences a fault or a dip in voltage, DG systems are designed to dynamically adjust their power output to support the point of common coupling (PCC) and ride through the voltage deviation. This capability, known as low-voltage ride-through (LVRT) [9], [10], [11], [12], has become a crucial requirement for the DG systems to facilitate seamless integration, ensuring that DG units remain connected during voltage sags. The most widely implemented approach for LVRT is to control the inverter to regulate the reactive power injection [13], [14], [15], [16], [17]. This method plays a pivotal role in stabilizing voltage levels and supporting grid integrity during disturbances.

For instance, Fig. 1(a) shows a three-phase grid-connected DG system, typically comprising multiple DG units, which can work in parallel in grid-following (GFL) or grid-forming (GFM) mode to supply power from the distributed sources (DSs) to

TABLE I
TRADITIONAL CURRENT REFERENCE GENERATORS

Traditional CRGs	$i_\alpha^\star$	$i_\beta^\star$	Strength	Drawback
IARC [23]	$\frac{3}{2}\left[\frac{P^\star(v_\alpha^+ + v_\alpha^-)}{D} + \frac{Q^\star(v_\beta^+ + v_\beta^-)}{D}\right]$	$\frac{3}{2}\left[\frac{P^\star(v_\beta^+ + v_\beta^-)}{D} - \frac{Q^\star(v_\alpha^+ + v_\alpha^-)}{D}\right]$	Elimination of power oscillation	Highly distorted current
AARC [24]	$\frac{3}{2}\left[\frac{P^\star(v_\alpha^+ + v_\alpha^-)}{\bar{D}} + \frac{Q^\star(v_\beta^+ + v_\beta^-)}{\bar{D}}\right]$	$\frac{3}{2}\left[\frac{P^\star(v_\beta^+ + v_\beta^-)}{\bar{D}} - \frac{Q^\star(v_\alpha^+ + v_\alpha^-)}{\bar{D}}\right]$	Elimination of current distortion	High power oscillation
BPSC [25]	$\frac{3}{2}\left[\frac{P^\star v_\alpha^+}{\bar{D}^+} + \frac{Q^\star v_\beta^+}{\bar{D}^+}\right]$	$\frac{3}{2}\left[\frac{P^\star v_\beta^+}{\bar{D}^+} - \frac{Q^\star v_\alpha^+}{\bar{D}^+}\right]$	Balanced and sinusoidal current	High power oscillation
PNSC [26]	$\frac{3}{2}\left[\frac{P^\star(v_\alpha^+ - v_\alpha^-)}{\bar{D}^+ - \bar{D}^-} + \frac{Q^\star(v_\beta^+ - v_\beta^-)}{\bar{D}^+ - \bar{D}^-}\right]$	$\frac{3}{2}\left[\frac{P^\star(v_\beta^+ - v_\beta^-)}{\bar{D}^+ - \bar{D}^-} - \frac{Q^\star(v_\alpha^+ - v_\alpha^-)}{\bar{D}^+ - \bar{D}^-}\right]$	Reduction of power oscillation, sinusoidal current	High unbalance in current
ICPS [27]	$\frac{3}{2}\left[\frac{P^\star v_\alpha^+}{\bar{D}+\tilde{D}} + \frac{Q^\star v_\beta^+}{\bar{D}+\tilde{D}}\right]$	$\frac{3}{2}\left[\frac{P^\star v_\beta^+}{\bar{D}+\tilde{D}} - \frac{Q^\star v_\alpha^+}{\bar{D}+\tilde{D}}\right]$	Reduction of power oscillation	High current distortion

(1) $i_\alpha^\star$ and $i_\beta^\star$ represent the α and β components of the current reference, respectively.
(2) $\bar{D} = \bar{D}^+ + \bar{D}^-$, $\bar{D}^+ = (v_\alpha^{+2} + v_\beta^{+2})$, $\bar{D}^- = (v_\alpha^{-2} + v_\beta^{-2})$, $\tilde{D} = (v_\alpha^+ v_\alpha^- + v_\beta^+ v_\beta^-)$, $D = \bar{D} + 2\tilde{D}$, while $^+$ and $^-$ represent the positive and negative sequence components, respectively.

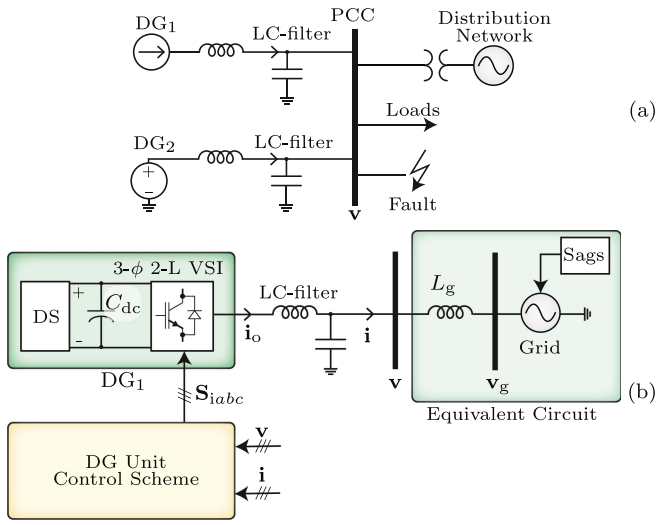

Fig. 1. Three-phase grid-connected DG system. (a) Circuit configuration. (b) The equivalent circuit and control scheme for DG_1.

the main distribution network and the local loads. Here, DG_1 implementing a GFL inverter serves as a controlled current source while DG_2 functions as a controlled voltage source with the inverter working in GFM mode. This research focuses on the GFL mode, which is commonly used in such configurations due to its straightforward implementation and grid compliance. Owing to the parallel operation, when a fault occurs at the PCC, individual DG units and their control scheme should be properly designed according to the equivalent condition of the PCC voltage. Thus, as depicted in the equivalent circuit shown in Fig. 1(b), the components beyond the PCC from the DG_1 perspective can be represented by a simplified grid model, where the voltage sag is part of the equivalent circuit. In response, the individual DG unit, e.g., DG_1 working in GFL mode, delivers the required power by following a suitable current reference $\mathbf{i}^\star$ for the injected current $\mathbf{i}$. This current is managed by the DG Unit Control Scheme in accordance with a desired current reference generator (CRG) that targets several system demands, e.g., current imbalance and distortion, and power oscillation (see Table I).

In general, the main characteristics of power and current during different voltage sags, as summarized in [18] and [19], highlight the significant efforts made to mitigate the adverse effects of unbalanced grid conditions, where unbalanced currents and oscillating power severely degrade power quality [20], [21], [22]. The traditional CRGs) for unbalanced operation are reported in [23], [24], [25], [26], and [27]. They are known as instantaneous active and reactive control (IARC), average active and reactive control (AARC), instantaneously controlled positive-sequence (ICPS), positive-and negative-sequence control (PNSC), and balanced positive-sequence control (BPSC). The main strengths and drawbacks are summarized in Table I. Note that, the performance requirement, i.e., constant powers, balanced current, and reduced harmonic distortion can be individually achieved by these traditional CRGs. However, standard CRGs are typically designed to optimize individual performance objectives separately, without accounting for tradeoffs or interactions with other metrics. As a result, nonprioritized metrics may exceed acceptable limits.

In [23], different traditional CRGs are applied to inject active power during grid faults. However, for simplicity, reactive power injection is assumed to be zero, which limits the voltage support during voltage sags. Pola et al. [28] introduced a comprehensive IARC (C-IARC) to transition between sinusoidal current and minimized power oscillations. However, the balance of the three-phase current is left uncontrolled. A current reference that regulates the positive and negative sequence of the current

flexibly during unbalanced sag conditions is proposed in [29]. Then, in [30], the control parameters are selected to eliminate the active power ripple, yet leaving the reactive power ripple unregulated. Moreover, to suppress the THD, this flexible positive and negative sequence current injection neglects the oscillation term caused by the cross-interaction of the different sequences. However, this inherently compromises the integrity of the current injection and lacks a direct connection with the traditional CRGs. Castilla et al. [31] introduced two decision variables to regulate the oscillation in power and current. But the algorithm can only govern two of the three performance metrics, e.g., Δp and Δq, leaving the other one, e.g., THD, uncontrollable. Thus, despite advancements in addressing unbalanced conditions, balancing the tradeoffs between current and power performance in CRGs remains a challenge.

Based on the above discussion, this article proposes a many-objective optimized current reference generation strategy (MaO-OCRGS). The design includes the addition of two decision variables into the CRG, which aim to combine the advantages of the traditional CRGs described above, thus governing three performance metrics, i.e., THD and Δp, Δq, but also introducing a fourth metric, defined as the *unbalance index* (UI) to provide a more comprehensive assessment of system performance during unbalanced voltage sags. This CRG was first presented in a conference paper [32]. The selection of the decision variables was not yet discussed in detail. This selection starts with the characterization of the relationship between decision variables and the performance metrics, since modifying the variables directly alters the metric values. The relationship for the power-related performance metrics (Δp and Δq) is theoretically derived. However, the effect of these decision variables on the current behavior, i.e., THD and UI cannot be established using straightforward analytical expressions. To address this challenge, an artificial neural network (ANN)-based current behavior model is proposed. ANNs effectively model complex, nonlinear relationships while substantially reducing computational burden through efficient training [33] and are widely used in power electronics [34], [35], [36], [37]. Unlike traditional methods, which struggle with complex relationships and require manual feature design, ANNs automatically learn patterns, offering greater accuracy and scalability. The theoretical power oscillation and the trained ANN-based current behavior model construct hybrid physics-based and data-driven (HPD) performance objective functions that evaluate all the aforementioned performance metrics, which are used to formulate the many-objective optimization (MaOO) problem. An optimal solution set that provides optimized tradeoffs between competing objectives is then obtained through optimization, from which the final optimal decision variables are determined through a postoptimization selection algorithm, leading to the optimized CRGs. Unlike traditional CRGs, which typically adopt a multimode optimization approach, this process performs a true multiobjective optimization. More specifically, the formulated problem considers four conflicting performance metrics within a unified framework, enabling the evaluation of tradeoffs. This optimization is conducted offline using a nondominated sorting algorithm III (NSGA-III), a powerful MaOO algorithm capable of handling complex objective functions and large search spaces. This algorithm has demonstrated superiority over other optimization approaches by maintaining strong diversity, robust convergence and higher computational efficiency in dealing with MaOO problems [38], [39], [40], [41]. Unlike NSGA-II and the strength Pareto evolutionary algorithm 2 (SPEA2), which struggle with maintaining diversity and performance as the number of objectives increases, NSGA-III uses a reference point-based mechanism that ensures a better distribution of solutions across the Pareto front without the need for objective weighting. Additionally, while algorithms like particle swarm optimization (PSO) can suffer from premature convergence and difficulty in exploring the search space, NSGA-III's elitist selection and structured reference points improve both convergence and diversity, making it more effective for MaOO problems.

Therefore, the main contributions of this work are summarized as follows.

1) To propose an MaO-OCRGS for DG systems under unbalanced voltage sags, integrating features from traditional CRGs i.e., IARC, AARC, ICPS, PNSC, and BPSC.
2) To enhance the overall LVRT performance of CRGs considering THD, Δp, Δq, and UI while maintaining them within predefined limits with the optimized CRGs obtained via the proposed MaO-OCRGS.
3) To demonstrate that the proposed strategy, combining the proposed HPD performance objective functions with NSGA-III-based optimization offers potential for addressing MaOO problems in CRGs design for LVRT support.

The rest of this article is organized as follows. Section II discusses the main components of the DG unit control scheme for LVRT support. Section III introduces the proposed CRG. Section IV formulates the MaOO problem using HPD performance objective functions. Section V describes the NSGA-III-based optimization for the decision variables of the proposed current reference. Section VI investigates a case study where the optimal decision variables are selected using the proposed MaO-OCRGS through simulation while the experimental validation of the proposed strategy is presented in Section VII. Finally, Section VIII concludes this article.

II. DG Unit Control Scheme for LVRT Support

Let us investigate the current injection and power delivery mechanisms in the DG system shown in Fig. 1. The instantaneous inverter output current, $\mathbf{i}_{\mathrm{o}}$, PCC voltage $\mathbf{v}$, injected current $\mathbf{i}$, and grid voltage $\mathbf{v}_{\mathrm{g}}$ vectors are denoted as

$$\mathbf{i}_{\mathrm{o}} = \begin{bmatrix} i_{\mathrm{o}a} & i_{\mathrm{o}b} & i_{\mathrm{o}c} \end{bmatrix}^T \tag{1a}$$

$$\mathbf{v} = \begin{bmatrix} v_a & v_b & v_c \end{bmatrix}^T \tag{1b}$$

$$\mathbf{i} = \begin{bmatrix} i_a & i_b & i_c \end{bmatrix}^T \tag{1c}$$

$$\mathbf{v}_{\mathrm{g}} = \begin{bmatrix} v_{\mathrm{g}a} & v_{\mathrm{g}b} & v_{\mathrm{g}c} \end{bmatrix}^T. \tag{1d}$$

Expressed in the stationary two-axis form by the $\alpha\beta$ transformation, the three-phase vectors are transformed from abc to $\alpha\beta$

as follows:

$$\mathbf{i}_{o\alpha\beta} = \begin{bmatrix} i_{o\alpha} & i_{o\beta} \end{bmatrix}^T = \left[\mathbf{\Gamma}_{\alpha\beta}^{abc}\right] \mathbf{i}_o \tag{2a}$$

$$\mathbf{v}_{\alpha\beta} = \begin{bmatrix} v_\alpha & v_\beta \end{bmatrix}^T = \left[\mathbf{\Gamma}_{\alpha\beta}^{abc}\right] \mathbf{v} \tag{2b}$$

$$\mathbf{i}_{\alpha\beta} = \begin{bmatrix} i_\alpha & i_\beta \end{bmatrix}^T = \left[\mathbf{\Gamma}_{\alpha\beta}^{abc}\right] \mathbf{i} \tag{2c}$$

$$\mathbf{v}_{g\alpha\beta} = \begin{bmatrix} v_{g\alpha} & v_{g\beta} \end{bmatrix}^T = \left[\mathbf{\Gamma}_{\alpha\beta}^{abc}\right] \mathbf{v}_g \tag{2d}$$

where $[\mathbf{\Gamma}_{\alpha\beta}^{abc}]$ is the $\alpha\beta$-transformation.

According to the instantaneous power theory [42], the instantaneous active and reactive power delivered to the PCC point, i.e., $p_{3\phi}$ and $q_{3\phi}$, can be expressed in terms of the PCC voltage and injected current, such that

$$\begin{bmatrix} p_{3\phi} \\ q_{3\phi} \end{bmatrix} = \frac{3}{2} \begin{bmatrix} v_\alpha & v_\beta \\ v_\beta & -v_\alpha \end{bmatrix} \begin{bmatrix} i_\alpha \\ i_\beta \end{bmatrix} = \frac{3}{2} \left[\mathbf{v}_{\alpha\beta}\right] \mathbf{i}_{\alpha\beta}. \tag{3}$$

In general cases, under balanced or unbalanced grid voltage, the grid voltage and current can be decomposed as follows:

$$\mathbf{v}_{\alpha\beta} = \mathbf{v}_{\alpha\beta}^+ + \mathbf{v}_{\alpha\beta}^- \tag{4a}$$

$$\mathbf{i}_{\alpha\beta} = \mathbf{i}_{\alpha\beta}^+ + \mathbf{i}_{\alpha\beta}^- \tag{4b}$$

where the signs $+$ and $-$ represent the positive and negative sequences of the corresponding vectors, consisting of $\alpha\beta$ components. Taking (4) into (3), active and reactive power can be expressed as

$$p_{3\phi} = p + \tilde{p} \tag{5a}$$

$$q_{3\phi} = q + \tilde{q} \tag{5b}$$

where

$$p = v_\alpha^+ i_\alpha^+ + v_\beta^+ i_\beta^+ + v_\alpha^- i_\alpha^- + v_\beta^- i_\beta^- \tag{6a}$$

$$\tilde{p} = v_\alpha^+ i_\alpha^- + v_\beta^+ i_\beta^- + v_\alpha^- i_\alpha^+ + v_\beta^- i_\beta^+ \tag{6b}$$

$$q = v_\beta^+ i_\alpha^+ + v_\beta^- i_\beta^- - v_\alpha^+ i_\beta^+ - v_\alpha^- i_\beta^- \tag{6c}$$

$$\tilde{q} = v_\beta^+ i_\alpha^- + v_\beta^- i_\alpha^+ - v_\alpha^+ i_\beta^- - v_\alpha^- i_\beta^+. \tag{6d}$$

The instantaneous active power $p_{3\phi}$ and reactive power $q_{3\phi}$ can be decomposed into two distinct components: the constant components p and q, which emerge from the interaction of identical current and voltage sequence components, and the oscillating components $\tilde{p}$ and $\tilde{q}$, which arise from the interaction of different sequence components.

To guarantee the aforementioned power transfer during both normal operation and voltage sag conditions, the DG unit control scheme, incorporating LVRT capability, comprises three key components: sequence extraction and grid estimation, CRG, and current controller.

A. Sequence Extraction and Grid Estimation

As demonstrated in Table I, the generation of the current reference involves the sequence extraction of the PCC voltage, which is performed by a sequence separation method (SSM). In this article, delayed signal cancellation (DSC) [43] is employed to calculate the positive sequence and negative sequence

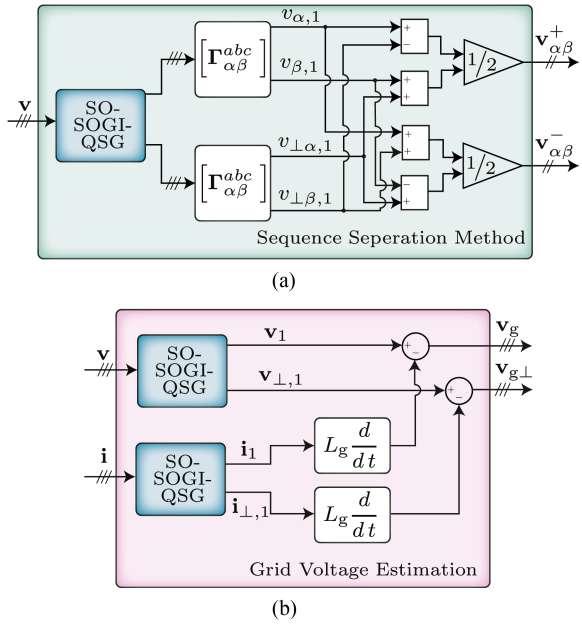

Fig. 2. SOGI-QSG. (a) SSM applying SO-SOGI-QSG and (b) grid voltage estimation.

$$\mathbf{v}_{\alpha\beta}^+ = \left[\mathbf{\Gamma}_{\alpha\beta}^{abc}\right] \mathbf{v}_{abc}^+ = \left[\mathbf{\Gamma}_{\alpha\beta}^{abc}\right] \left[\mathbf{\Gamma}_+\right] \left[\mathbf{\Gamma}_{\alpha\beta}^{abc}\right]^T \mathbf{v}_{\alpha\beta,1} \tag{7a}$$

$$= \frac{1}{2} \begin{bmatrix} 1 & -\perp \\ \perp & 1 \end{bmatrix} \mathbf{v}_{\alpha\beta,1}$$

$$\mathbf{v}_{\alpha\beta}^- = \left[\mathbf{\Gamma}_{\alpha\beta}^{abc}\right] \mathbf{v}_{abc}^- = \left[\mathbf{\Gamma}_{\alpha\beta}^{abc}\right] \left[\mathbf{\Gamma}_-\right] \left[\mathbf{\Gamma}_{\alpha\beta}^{abc}\right]^T \mathbf{v}_{\alpha\beta,1}$$

$$= \frac{1}{2} \begin{bmatrix} 1 & \perp \\ -\perp & 1 \end{bmatrix} \mathbf{v}_{\alpha\beta,1} \tag{7b}$$

where $[\mathbf{\Gamma}_+]$ and $[\mathbf{\Gamma}_-]$ represent the positive and negative sequence operation, respectively. $\mathbf{v}_{\alpha\beta,1}$ represents the fundamental component of $\mathbf{v}_{\alpha\beta}$. Multiplying the operator $\perp$ by any signal, e.g., $\perp v_{\alpha,1}$, represents a delayed version of the original signal, shifted by $\pi/2$, i.e., yielding $v_{\alpha\perp,1}$, which can be obtained with a second-order generalized integrator (SOGI). The SOGI is an effective solution for filtering and shifting which serves as a quadrature signal generator (QSG) [44]. As per [44], its in-phase output and quadrature output closely approximate sine waves, the fundamental components, v_1 and $v_{\perp,1}$. Here, a second-order SOGI-QSG (SO-SOGI-QSG) is used to ensure reliable filtering. Fig. 2(a) illustrates the structure and the implementation of the SSM employing the SO-SOGI-QSG. As will be discussed later, the dynamic performance of the sequence extraction method is not expected to significantly affect the CRG operation, then the gain parameters of the SO-SOGI-QSG (see [45] for k_{SOGI1} and k_{SOGI2}) are set to provide a balance between dynamic response and filtering capability [31].

The operational mode of the DG unit control scheme, whether during normal operation or voltage sag conditions, is determined by the grid voltage status. Although direct measurement of the

grid voltage is not feasible, it can be estimated using the PCC voltage and the injected current as

$$\mathbf{v}_{\mathrm{g}} = \mathbf{v} - L_{\mathrm{g}}\frac{d\,\mathbf{i}}{d\,t} \tag{8a}$$

$$\mathbf{v}_{\mathrm{g}\perp} = \mathbf{v}_{\perp} - L_{\mathrm{g}}\frac{d\,\mathbf{i}_{\perp}}{d\,t} \tag{8b}$$

where $\mathbf{v}_{\perp}$, $\mathbf{v}_{\mathrm{g}\perp}$, and $\mathbf{i}_{\perp}$ are the 90° phase-shifted PCC voltage, grid voltage and injected current, respectively. And L_{g} is the equivalent grid inductance. In this article, the root-mean-square (rms) value of an arbitrary variable x can be calculated using $\check{x} = \sqrt{(x_1^2 + x_{\perp,1}^2)/2}$. The rms value of the grid voltage is therefore readily obtained. In Fig. 2(b), the estimation of the grid voltage is shown in detail. Note that, although SO-SOGI-QSG considers the aforementioned filtering capability, in this article the grid is considered without harmonics. Thus, potential harmonics as well as a nonideal grid impedance, e.g. L_g, is considered beyond the scope of this work.

B. Current Reference Generator

From (4b), the injected current becomes distorted due to the presence of negative sequence components introduced by an unbalanced fault, which, as indicated by (6c) and (6d), also leads to power oscillations caused by the interaction of negative sequence components in the injected current and voltage. These oscillations can negatively impact the grid [46]. Although the voltage components of the grid remain uncontrollable, the current components injected can be effectively regulated through a suitable CRG in combination with a current controller, which ensures that the injected current adheres to its current references. As described in Table I, while numerous CRGs have been developed, achieving specific performance objectives often requires compromising other aspects of system performance, which causes tradeoffs. To deal with these tradeoffs in the traditional CRGs, in this article, the current reference for the DG unit control scheme is generated by following the procedure of the proposed MaO-OCRGS, which consists of the proposed current reference, the MaOO problem, and the proposed NSGA-III-based current reference optimization. The detailed implementation of each step is provided in the next sections.

C. Current Controller

A model predictive control (MPC) is selected as the current controller due to its fast response and reliable dynamic performance required by the reference change between normal operation and sag conditions. Unlike many studies that focus on controlling the inverter output current $\mathbf{i}_{\mathrm{o}}$, this MPC controller directly governs the injected current $\mathbf{i}$. Consequently, the injected current is predicted with

$$\begin{aligned}\mathbf{i}_{\alpha\beta}(k+1) &= \mathbf{A}_1(3,1)\mathbf{i}_{\mathrm{o}\alpha\beta}(k) + \mathbf{A}_1(3,2)\mathbf{v}_{\alpha\beta}(k)\\ &+ \mathbf{A}_1(3,3)\mathbf{i}_{\alpha\beta}(k) + \mathbf{B}_1(3,1)\mathbf{v}_0(k) + \mathbf{B}_2(3,1)\mathbf{v}_{\mathrm{g}\alpha\beta}(k)\end{aligned} \tag{9}$$

where $\mathbf{A}_1 = e^{AT_s}, \mathbf{B}_1 = \int_0^{T_s} e^{\mathbf{A}\tau}\mathbf{B}\,d\tau, \mathbf{B}_2 = \int_0^{T_s} e^{\mathbf{A}\tau}\mathbf{B}_d\,d\tau$. Matrices $\mathbf{A}$, $\mathbf{B}$, and $\mathbf{B_d}$ are formed as

$$\mathbf{A} = \begin{bmatrix} 0 & -1/L_{\mathrm{f}} & 0 \\ 1/C & 0 & -1/C \\ 0 & 1/L_{\mathrm{g}} & 0 \end{bmatrix}, \mathbf{B} = \begin{bmatrix} 1/L_{\mathrm{f}} \\ 0 \\ 0 \end{bmatrix}, \mathbf{B}_d = \begin{bmatrix} 0 \\ 0 \\ -1/L_{\mathrm{g}} \end{bmatrix}$$

where L_{f} and C denote the inductance and the capacitance of the *LC* filter, respectively.

Note that the injected current $\mathbf{i}_{\alpha\beta}$ and capacitor voltage $\mathbf{v}_{\alpha\beta}$ are measured. The dc side voltage V_{dc} is assumed to be constant, and the inverter current can be estimated as

$$\mathbf{i}_{\mathrm{o}\alpha\beta}(k) = \mathbf{i}_{\alpha\beta}(k) + C/Ts \cdot [\mathbf{v}_{\alpha\beta}(k) - \mathbf{v}_{\alpha\beta}(k-1)]\,. \tag{10}$$

The cost function, which states the error between the injected current $\mathbf{i}_{\alpha\beta}$ and the proposed reference $\mathbf{i}^{\star}_{\alpha\beta}$, is calculated for each switch combination as

$$g = (i_\alpha - i^{\star}_\alpha)^2 + (i_\beta - i^{\star}_\beta)^2. \tag{11}$$

Finally, the optimal switching combination is chosen to be the one that minimizes the cost function g

$$\mathbf{S}_{\mathrm{i}abc} = \mathrm{argmin}(g) \tag{12}$$

where $\mathbf{S}_{\mathrm{i}abc} = [S_{\mathrm{i}a}\ \ S_{\mathrm{i}b}\ \ S_{\mathrm{i}c}]^T$. $S_{\mathrm{i}\phi}$ is the inverter switching signal of phase ϕ, indicating the ON/OFF state of the corresponding switch. Specifically, $S_{\mathrm{i}\phi} = 1$ corresponds to the upper switch being ON and the lower switch being OFF, while $S_{\mathrm{i}\phi} = 0$ indicates the opposite configuration.

III. Proposed Current Reference Generator

In this section, the output of the CRG, i.e, current reference, is defined for both normal operation and voltage sag conditions. The aim is to unify the traditional CRGs by analyzing their tradeoffs and integrating their characteristics. First, rather than following predefined LVRT control strategies, the power references $P^{\star}$ and $Q^{\star}$, which are then embedded in the current reference, are determined according to the rated apparent power $S^{\star}$ based on the following expression (originally proposed in [32] with detailed derivations):

$$Q^{\star} = \begin{cases} 0 & , \Delta\check{v}_{\mathrm{sag}}\% \le 0.1 \\ \dfrac{\left(\sqrt{S^{\star 2}\cdot(X_{\mathrm{g}}^2+1) - \Delta\check{v}_{\mathrm{sag}}{}^2\cdot V_{\mathrm{g}}^2} + \Delta\check{v}_{\mathrm{sag}}\cdot X_{\mathrm{g}}\cdot V_{\mathrm{g}}\right)}{X_{\mathrm{g}}^2+1} & , \Delta\check{v}_{\mathrm{sag}}\% > 0.1 \end{cases}$$

$$P^{\star} = \sqrt{S^{\star 2} - Q^{\star 2}} \tag{13}$$

where $\Delta\check{v}_{\mathrm{sag}}$ is the voltage sag, defined as the difference between the nominal grid voltage V_{g} and the voltage at the sag phase $\check{v}_{\mathrm{sag}}$, i.e., $\Delta\check{v}_{\mathrm{sag}} = V_{\mathrm{g}} - \check{v}_{\mathrm{sag}}$. Its percentage form is given by $\Delta\check{v}_{\mathrm{sag}}\% = \Delta\check{v}_{\mathrm{sag}}/V_{\mathrm{g}}$. R_{g} and X_{g} are the resistance and reactance of the transmission line. Note that the current amplitude can be calculated as $I = \frac{\sqrt{2}S^{\star}}{3\check{v}}$, where $\check{v} = \sqrt{(v_\alpha^2 + v_\beta^2)/2}$. During a severe voltage sag, $\check{v}$ decreases significantly, potentially leading to an excessive increase in current if the apparent power reference $S^{\star}$ remains unchanged. To prevent this, a current limit is added to constrain the current by adjusting the apparent power when the current amplitude $I > I_{\mathrm{limit}}$. Since the current

TABLE II
DECISION VARIABLES SETTING FOR TRADITIONAL CRGS

CRG	IARC	AARC	PNSC	BPSC	ICPS
c_1	1.0	0.0	0.0	0.0	0.5
c_2	1.0	1.0	-1.0	0.0	0.0

amplitude is directly related to the apparent power, constraining the apparent power to $S_{\text{limit}} = 3I_{\text{limit}}\check{v}/\sqrt{2}$ ensures that the resulting current does not exceed I_{limit}, i.e., $I = \frac{\sqrt{2}S_{\text{limit}}}{3\check{v}} = \frac{\sqrt{2}(3I_{\text{limit}}\check{v})}{3\sqrt{2}\check{v}} = I_{\text{limit}}$. Otherwise, when $I \leq I_{\text{limit}}$, the apparent power follows its reference value $S^\star$. The aforementioned current constraint is implemented by modifying the active and reactive power references as $P^\star = \frac{\min(S^\star, S_{\text{limit}})}{S^\star}P^\star$, $Q^\star = \frac{\min(S^\star, S_{\text{limit}})}{S^\star}Q^\star$.

Then, the current references $i^\star_\alpha$ and $i^\star_\beta$ (see Table I) can be defined using voltage sequences as in (7) and the power references as in (13), considering the current limit described above. However, as discussed before, the main drawback is the tradeoff nature of the traditional CRGs. For instance, comparing IARC with AARC, AARC generates a sinusoidal current waveform with oscillated power by removing the oscillating term $\tilde{D}$. In contrast, IARC can eliminate power oscillations, but at the expense of a distorted current. The extreme characteristics of AARC and IARC can be mitigated by introducing a decision variable c_1 that adjusts the proportion of $\tilde{D}$ as

$$D_c = \bar{D} + 2c_1\tilde{D} \tag{14}$$

where c_1 varies between 0 and 1. This approach effectively balances the benefits and drawbacks of both IARC and AARC.

Comparing BPSC, ICPS, and PNSC, a decision variable c_2 ranging from -1 to 1 is further introduced to change the participation of the negative sequence component, thereby influencing current balancing

$$\mathbf{v}^+_{\alpha\beta} + c_2 \cdot \mathbf{v}^-_{\alpha\beta}. \tag{15}$$

By incorporating c_2, (14) is updated as follows:

$$D_c = \bar{D}^+ + c_2 \cdot \bar{D}^- + 2c_1\tilde{D}. \tag{16}$$

Thus, implementing the decision variables c_1 and c_2 as (15) and (16), this article proposes a current reference as

$$i^\star_\alpha = \frac{2}{3}\left[\frac{P^\star(v^+_\alpha + c_2 v^-_\alpha)}{\bar{D}^+ + c_2\bar{D}^- + 2c_1\tilde{D}} + \frac{Q^\star(v^+_\beta + c_2 v^-_\beta)}{\bar{D}^+ + c_2\bar{D}^- + 2c_1\tilde{D}}\right] \tag{17a}$$

$$i^\star_\beta = \frac{2}{3}\left[\frac{P^\star(v^+_\beta + c_2 v^-_\beta)}{\bar{D}^+ + c_2\bar{D}^- + 2c_1\tilde{D}} - \frac{Q^\star(v^+_\alpha + c_2 v^-_\alpha)}{\bar{D}^+ + c_2\bar{D}^- + 2c_1\tilde{D}}\right]. \tag{17b}$$

Note that the traditional CRGs can still be implemented by setting the decision variables as per Table II. The ranges of c_1 and c_2 are then determined as $0 \leq c_1 \leq 1$ and $-1 \leq c_2 \leq 1$, ensuring full coverage of all traditional CRGs through the proposed current reference (17).

IV. MANY-OBJECTIVE OPTIMIZATION PROBLEM

Since the decision variables c_1 and c_2 have yet to be determined, this section formulates an MaOO problem based on four power quality performance metrics. The first pair of performance metrics is classified as power-related metrics (Δp and Δq). They are used to quantify the active and reactive power ripple as

$$\Delta p = \frac{(p_{3\phi} - P^\star)_{\max}}{P^\star} \tag{18a}$$

$$\Delta q = \frac{(q_{3\phi} - Q^\star)_{\max}}{Q^\star}. \tag{18b}$$

The second pair of performance metrics is classified as current-related metrics, which are used to quantify the distortion and level of imbalance in the injected current. The current distortion is defined by the THD as

$$THD = \frac{1}{3}\sum_{\phi\in a,b,c}\frac{\sqrt{\check{i}^2_\phi - \check{i}^2_{\phi,1}}}{\check{i}_{\phi,1}} \tag{19}$$

where $\check{i}_\phi$ is the rms value of the phase ϕ current and $\check{i}^2_{\phi,1}$ is the rms value of its fundamental component of this phase current. Focusing on the performance during unbalanced voltage sags, an additional UI is introduced to evaluate the level of the imbalance in the three-phase current, i.e.,

$$UI = \frac{\max(|\check{i}_a - \check{i}_{\text{avg}}|, |\check{i}_b - \check{i}_{\text{avg}}, |\check{i}_c - \check{i}_{\text{avg}}|)}{\check{i}_{\text{avg}}} \tag{20}$$

where $\check{i}_a, \check{i}_b, \check{i}_c$ are the rms values of the injected current of phase a, b and c, respectively, and $\check{i}_{\text{avg}}$ is the average value of the rms value of the three-phase current.

Finally, based on the four established performance metrics, the next step in the proposed CRG strategy is to formulate an optimization problem to determine the optimal decision variables that optimize these metrics.

A. MaOO Problem Formulation

The optimization problem is formulated to minimize the performance metrics based on their equivalent objective functions, while ensuring that the decision variables satisfy the given boundaries, as follows:

$$\mathcal{P}_{\text{MaOO}}: \ \min \mathbf{f}(\mathbf{x}) = \min\left[f_1(\mathbf{x}), f_2(\mathbf{x}), f_3(\mathbf{x}), f_4(\mathbf{x})\right] \tag{21a}$$

$$\text{subject to } 0 \leq c_1 \leq 1, \quad -1 \leq c_2 \leq 1. \tag{21b}$$

The objective functions $f_1(\mathbf{x})$ and $f_2(\mathbf{x})$ characterize the power oscillations Δp and Δq, respectively. Similarly, the functions $f_3(\mathbf{x})$ and $f_4(\mathbf{x})$ quantify the THD and UI, both expressed as percentages. The decision vector $\mathbf{x}$ is composed of the decision variables, i.e., $\mathbf{x} = [c_1, c_2]$, with boundaries as per (21b).

B. Hybrid Physics-Based and Data-Driven Performance Objective Functions

The power-related objective functions $f_1(\mathbf{x})$ and $f_2(\mathbf{x})$ can be derived in a physical basis. Taking (17) into (18a) and (18b)

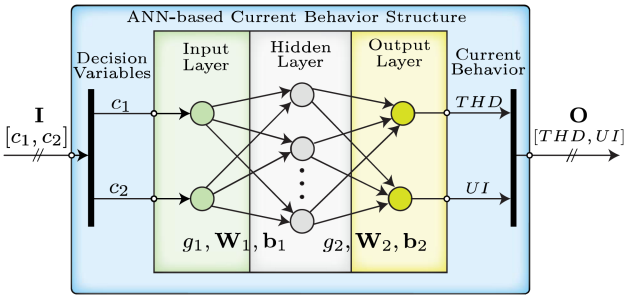

Fig. 3. ANN-based current behavior structure.

by inserting (3), the active power and reactive power oscillation are generalized as

$$\Delta p = \left[\frac{(1-2c_1+c_2)\cdot\lambda\cdot\cos(2\omega t+\varphi_v^+-\varphi_v^-)}{1+c_2\cdot\lambda^2+2c_1\cdot\lambda\cdot\cos(2\omega t+\varphi_v^+-\varphi_v^-)} - \frac{Q^\star/P^\star(c_2-1)\cdot\lambda\cdot\sin(2\omega t+\varphi_v^+-\varphi_v^-)}{1+c_2\cdot\lambda^2+2c_1\cdot\lambda\cdot\cos(2\omega t+\varphi_v^+-\varphi_v^-)} \right]_{\max} \tag{22a}$$

$$\Delta q = \left[\frac{(1-2c_1+c_2)\cdot\lambda\cdot\cos(2\omega t+\varphi_v^+-\varphi_v^-)}{1+c_2\cdot\lambda^2+2c_1\cdot\lambda\cdot\cos(2\omega t+\varphi_v^+-\varphi_v^-)} - \frac{P^\star/Q^\star(c_2-1)\cdot\lambda\cdot\sin(2\omega t+\varphi_v^+-\varphi_v^-)}{1+c_2\cdot\lambda^2+2c_1\cdot\lambda\cdot\cos(2\omega t+\varphi_v^+-\varphi_v^-)} \right]_{\max}. \tag{22b}$$

In (22), λ is the voltage unbalance factor, which indicates the degree of voltage unbalance and is expressed as

$$\lambda = \breve{v}^-/\breve{v}^+ \tag{23}$$

where $\breve{v}^+$ and $\breve{v}^-$ denote the rms value, φ_v^+ and φ_v^- represent the phase angles of the positive and negative sequence of the PCC voltage, respectively. Additionally, ω is the fundamental angular frequency of the system, and t is time.

The current-related performance objective functions in (21) have yet to be represented. As discussed in the Introduction, the generalization of the current-related metrics, THD and UI is not straightforward. To address this challenge, a data-driven approach is adopted, where an ANN is proposed to model the current-related objective functions $f_3(\mathbf{x})$ and $f_4(\mathbf{x})$.

The proposed ANN current behavior model features a hidden layer with 10 neurons positioned between the input layer and output layer. The input $\mathbf{I}$ is the decision vector $\mathbf{x}$ defined as $[c_1, c_2]$ and the output $\mathbf{O}$ corresponds to the current behavior performance metrics, expressed as $[THD, UI]$. This structure is illustrated in Fig. 3 with the following expressions:

$$\mathbf{H} = g_1\left(\mathbf{W_1}\mathbf{I} + \mathbf{b_1}\right) \tag{24a}$$

$$\mathbf{O} = g_2\left(\mathbf{W_2}\mathbf{I} + \mathbf{b_2}\right) \tag{24b}$$

where matrices $\mathbf{W_1}$ and $\mathbf{W_2}$ are the weighting matrices in the hidden and output layer, respectively, with corresponding bias matrices $\mathbf{b_1}$ and $\mathbf{b_2}$. The activation functions for the hidden and output layers are denoted by g_1 and g_2. Fig. 4 illustrates the training process of the ANN-based current behavior model.

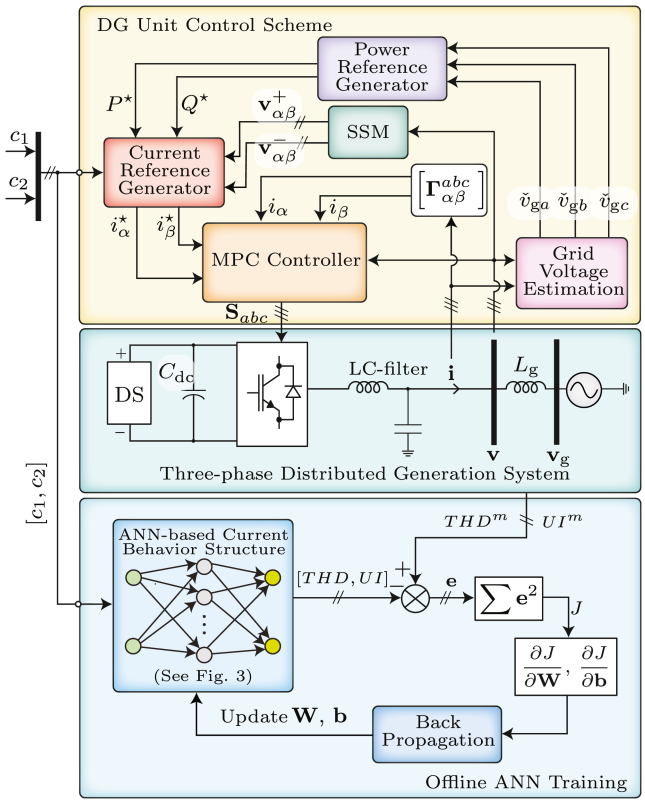

Fig. 4. ANN-based current behavior training.

The estimated grid voltage first detects the fault and then determines the power reference by (13). The current reference is then computed by the proposed CRG (17), incorporating the decision variables, power reference, and sequence components of the PCC voltage separated using the SSM method as (7). For each set of the decision variables c_1 and c_2, the controller governs the current to align it with the corresponding CRG. The error between ANN-predicted current behavior and the actual measurement (THD^m, UI^m) is then used to calculate the loss J. To minimize J, the weighting matrices $\mathbf{W}$ and bias vectors $\mathbf{b}$ are updated via backpropagation with their gradients, progressively fitting the ANN to the actual current behavior.

In the proposed approach, both physics-based and data-driven methodologies are integrated to determine the objective functions in the MaOO problem $\mathcal{P}_{\text{MaOO}}$ (21), constructing the HPD performance objective functions. Specifically, the physics-based model (22) is employed for $f_1(\mathbf{x})$ and $f_2(\mathbf{x})$, while the data-driven ANN structure (24) is used for $f_3(\mathbf{x})$ and $f_4(\mathbf{x})$. This HPD approach facilitates a comprehensive and accurate characterization of the performance objective functions.

V. NSGA-III-Based Current Reference Optimization

Finally, an NSGA-III-based current reference optimization algorithm illustrated in Fig. 5 is used to identify the optimal decision variables c_1 and c_2, thus determining the optimized CRGs. Though the tradeoffs among the performance

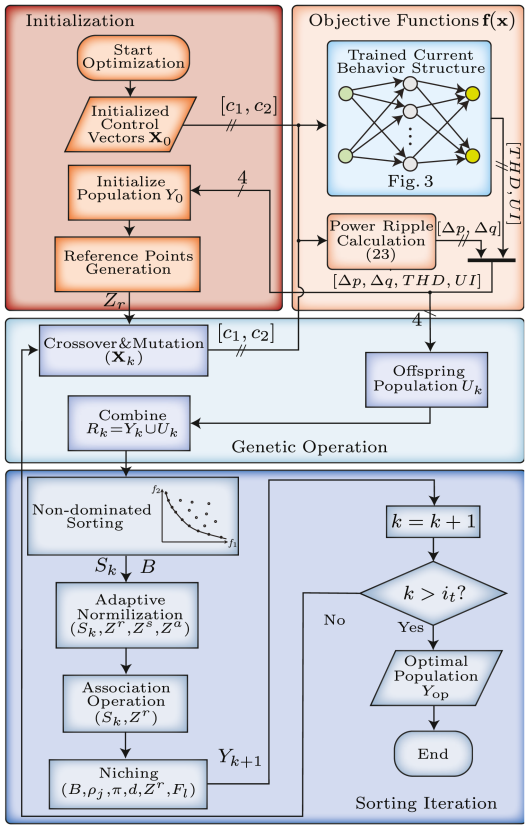

Fig. 5. NSGA-III optimization for obtaining the optimal population Y_{op}.

metrics prevent simultaneous improvement, a prioritized optimization is permitted. Two steps are involved: NSGA-III optimization, which identifies an optimal solution set that provides optimized tradeoffs between competing objectives, and the postoptimization selection, which seeks to enhance one performance metric without significant compromises in others, that is, while maintaining the others within predefined limits.

In general, solving (21) requires an initial population Y_0 to make a fair start. As Table II indicates, the values of c_1 and c_2 for the traditional CRGs cover the entire range. So here, to ensure that the algorithm explores all traditional CRGs during iterations, the initial population is distributed evenly around the ranges of the decision variables c_1 and c_2. Then in each iteration, a genetic operation process within the boundaries that includes mutation and crossover operators is applied to create the offspring population U_k [47], which is combined with the parental population Y_k as R_k. Each individual comprises the decision vectors $\mathbf{x}$ and the corresponding normalized objective functions $\mathbf{f}_{\text{norm}}(\mathbf{x})$, where the normalized values are obtained by applying min-max normalization to the performance metrics calculated from the proposed objective functions $\mathbf{f}(\mathbf{x})$. This normalization ensures balanced consideration of each metric during NSGA-III optimization while ensuring solution diversity and convergence. A sorting iteration process then begins to select N superior individual decision vectors from the combined population R_k.

First, all the individuals in the combined population R_k are ranked according to the Pareto optimal principle. Individual a dominates b if

$$\mathbf{f}_{\text{norm}}(\mathbf{x}_a) \leq \mathbf{f}_{\text{norm}}(\mathbf{x}_b) \tag{25}$$

indicating that all performance metrics of $\mathbf{x}_a$ are not greater than that of solution $\mathbf{x}_b$. Individuals are grouped into layers F_1, F_2,..., F_n according to the number of other individuals they dominate. The layers with high priority are retained until $|F_1 \cup F_2 \cup \ldots \cup F_{l-1}| < N$ while $|F_1 \cup F_2 \cup \ldots \cup F_l| > N$. Assuming $|F_1 \cup F_2 \cup \ldots \cup F_{l-1}| = A$, the rest $B = N - A$ individuals remain to be selected. The NSGA-II applies crowding distance while in NSGA-III, it is determined with the concept of reference point association. The detailed NORMALIZE, ASSOCIATE, and NITCHING procedure can be found in [38]. The aforementioned operations are executed until the predefined number of iterations i_t is reached, yielding the optimal population Y_{op}.

The final step is to select the optimal decision variables from the optimal population which consists of N sets of decision variable solutions, performing a postoptimization selection. Due to tradeoffs among performance metrics, no single solution minimizes all of them simultaneously. Consequently, it is infeasible to enhance one performance metric while keeping the others strictly noninferior. Therefore, the final solution is selected based on a prioritization rule: one performance metric is prioritized while ensuring that the others remain within predefined limits. Note that, in this process, the improvement in one performance metric is still achieved at the expense of other metrics, albeit in a constrained manner where all degraded metrics remain within predefined limits. Moreover, all selected decision variable solutions originate from the true multiobjective optimization achieved through NSGA-III and thus inherently capture the tradeoffs among competing performance metrics. As a result, the selected decision variables define the optimized CRGs, named according to their prioritized objectives: OTHD for optimized THD, OUI for optimized UI, ORA for optimized active power ripple, and ORR for optimized reactive power ripple. These optimized CRGs fundamentally differs from traditional CRGs developed through multimode optimization, which treats each performance aspect separately, without accounting for their interactions. This process is coded as Algorithm 1, while the overall strategy, i.e., the proposed MaO-OCRGS, which includes the steps described in Sections III–V, is summarized in Algorithm 2.

VI. Simulation Results

To determine the optimized CRGs using the proposed MaO-OCRGS described in the previous sections, a grid-connected DG system as shown in Fig. 1, consisting of a DS with VSI, *LC* filter, an equivalent grid and the DG unit control scheme, is simulated in MATLAB/Simulink with the parameters listed in Table III. For instance, a Type B voltage sag (30% single-phase voltage dip) is taken as a case study. The optimal decision variables and thus the optimized CRGs are obtained by following the aforementioned proposed MaO-OCRGS as Algorithm 2. The results are presented as follows. Note that the proposed strategy is applicable to sag types beyond the case study, enabling the determination of optimized CRGs for diverse sag conditions.

Algorithm 1: Selection of Optimized Current Reference Generators.

Input: Optimal population Y_{OP}, Limits for performance metrics THD_{limit}, UI_{limit}, Δp_{limit}, Δq_{limit}
Output: OTHD, OUI, ORA, ORR

Initialize: $\text{THD}_{\min} \leftarrow \infty$, $\text{UI}_{\min} \leftarrow \infty$, $\Delta p_{\min} \leftarrow \infty$, $\Delta q_{\min} \leftarrow \infty$
  $i_{\text{THD}} \leftarrow 1$, $i_{\text{UI}} \leftarrow 1$, $i_{\Delta p} \leftarrow 1$, $i_{\Delta q} \leftarrow 1$
for $i = 1$ **to** $|Y_{\text{OP}}|$ **do**
  if $Y_{\text{OP}}[i].\text{PM} < \text{PM}_{\text{limit}}$ for all PM $\in \{\text{THD}, \text{UI}, \Delta p, \Delta q\}$ **then**
    for each PM $\in \{\text{THD}, \text{UI}, \Delta p, \Delta q\}$ **do**
      if $Y_{\text{OP}}[i].\text{PM} < \text{PM}_{\min}$ **then**
        $\text{PM}_{\min} \leftarrow Y_{\text{OP}}[i].\text{PM}$
        $i_{\text{PM}} \leftarrow i$
      end if
    end for
  end if
end for
OTHD $\leftarrow Y_{\text{OP}}[i_{\text{OTHD}}]$, OUI $\leftarrow Y_{\text{OP}}[i_{\text{OUI}}]$, ORA $\leftarrow Y_{\text{OP}}[i_{\text{ORA}}]$, ORR $\leftarrow Y_{\text{OP}}[i_{\text{ORR}}]$

Algorithm 2: Proposed Many-Objective Optimized Current Reference Generation Strategy.

/* Proposed Current Reference Generator */
$[P^\star, Q^\star] \leftarrow$ Power Reference Generator$(\Delta \check{v}_{\text{sag}})$ /*(13)*/
$[i^*_\alpha, i^*_\beta] \leftarrow$ Current Reference$(c_1, c_2, v^+_\alpha, v^+_\beta, v^-_\alpha, v^-_\beta, P^\star, Q^\star)$ /*(17)*/
/* Many-Objective Optimization Problem */
$[f_1(\mathbf{x}), f_2(\mathbf{x}), f_3(\mathbf{x}), f_4(\mathbf{x})] \leftarrow$ Proposed Hybrid Physics-based and Data-driven Performance Objective Functions /*(22), Fig. 4*/
$\mathcal{P}_{\text{MaOO}} \leftarrow$ MaOO Problem Formulation /*(21)*/
/* NSGA-III-based Current Reference Optimization */
$Y_{\text{op}} \leftarrow$ NSGA-III Optimization /*Fig. 5*/
[OTHD, OUI, ORAR] $\leftarrow$ Selection of Optimized Current Reference Generators /*Algorithm 1*/

A. ANN-Based Current Behavior Training Results

Training the proposed ANN-based current behavior model requires a representative data set comprising the decision variables and the values of their corresponding performance metrics. Here, the decision variables are discretized with a step size of 0.025 over the ranges $0 \leq c_1 \leq 1$ and $-1 \leq c_2 \leq 1$ with a step of 0.025, which ensures sufficient resolution while maintaining computational efficiency. For each combination of decision variables, the corresponding current reference determined using (17) is implemented to the developed simulation model. The resulting performance metrics obtained from the simulation are recorded, forming a comprehensive dataset of 3321 samples. Fig. 6 shows the variation of the four performance metrics across the decision variables c_1 and c_2.

TABLE III
PARAMETERS FOR EXPERIMENTAL AND SIMULATION SETUP

Description	Symbol	Value
DG System Parameters		
Grid voltage, rms line-ground	V_{g}	110 V
Rated apparent power	$S^\star$	2.5 kVA
Grid frequency	f	50 Hz
dc-link capacitance	C_{dc}	3.3 mF
LC-Filter inductance	L_{f}	6 mH
LC-Filter capacitance	C	0.22 μf
Grid inductance	L_{g}	6.8 mH
Grid simulator	ACS	MODEL 61830
DC supply	DCS	IT6006C-800-20
Avg. switching freq.	f_{sw}	22.58 kHz
SO-SOGI QSG Parameters		
First integrator gain	k_{SOGI1}	1.56
Second integrator gain	k_{SOGI2}	3.11
ANN Parameters		
Discretization step	d_s	0.025
Number of hidden neurons	N_{neu}	6
Minimal gradient	ϵ_{grad}	1×10^{-7}
Maximal regularization	$\mu_{\max}$	1×10^{10}
NSGA-III Parameters		
Population size	N	80
Division number	d	3
Iteration number	i_t	200
Crossover rate	r_c	0.7
Mutation rate	r_m	0.5
Search step	h_s	0.001
Control Parameters		
Sampling time	T_s	25 μs
Turn around time	T_{ta}	9.27 μs
Simulation platform	Matlab/Simulink	2021a/10.2
Digital control platform	dSPACE	ds1202
FPGA clock frequency	f_{clk}	100 MHz

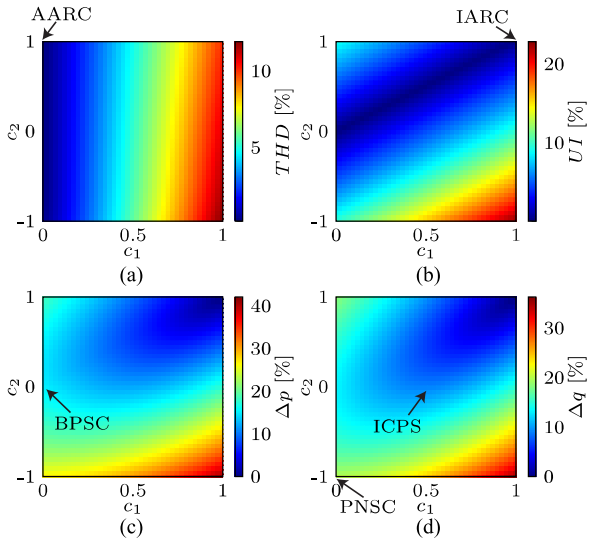

Fig. 6. Performance metrics varying with different values of decision variables under a type B voltage sag. (a) THD, (b) UI, (c) active power ripple Δp, and (d) reactive power ripple Δq.

According to Fig. 6(a), (c), and (d), when c_2 is fixed at 1 and c_1 varies from 0 to 1, a clear transition in performance occurs from the AARC to IARC CRGs with an increase in THD alongside a reduction in power ripple. When c_1 remains constant at 0, the current progressively balances as the negative component

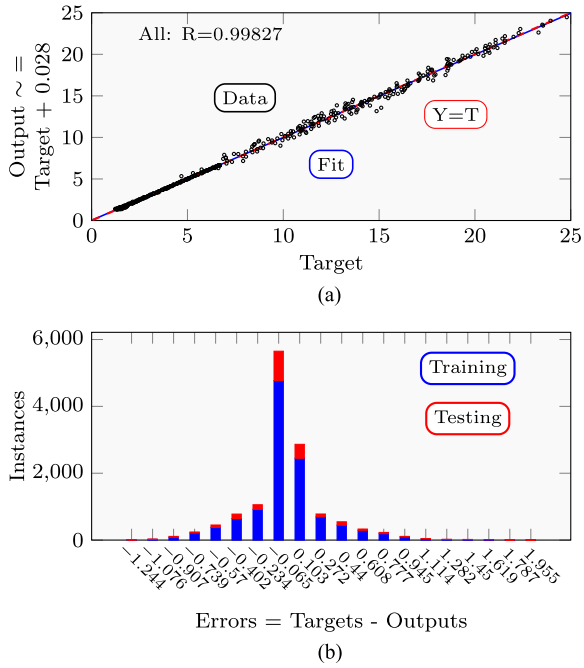

Fig. 7. ANN training results. (a) Training regression. (b) Error histogram.

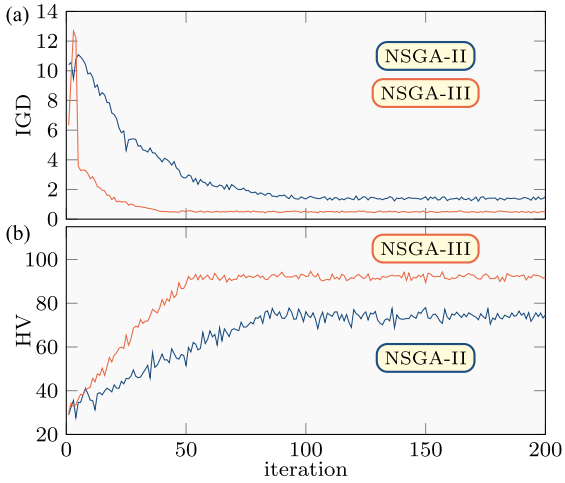

Fig. 8. Comparison of performance metrics (a) IGD and (b) HV between NSGA-III and NSGA-II on the formulated MaOO problem.

decreases, ultimately achieving BPSC and eliminating any imbalance as c_2 approaches 0.

Next, the recorded current-related performance metrics THD and UI of the simulation dataset are employed for the ANN training shown in Fig. 4, with the dataset partitioned into training (80%) and test (20%) subsets to ensure rigorous validation. The Levenberg-Marquardt backpropagation (BP) method is employed to train the current behavior ANN. The convergence criteria are met when either the gradient falls below 1×10^{-7}, indicating the error is acceptable with limited further improvement, or the regularization parameter μ reaches its maximum value of 1×10^{10}, suggesting that further iteration is constrained by over-regularization. The training regression results are shown in Fig. 7(a). The output and target data are recorded from both the training and the test, showing that the fitting line nearly overlaps with the line of identity "Y=T," achieving a correlation coefficient of 0.99827, which indicates a strong correlation and affirms the model's effectiveness in accurately capturing current behavior. Fig. 7(b) shows that most errors between the target and output values are centered around -0.06519, further validating the accuracy of the trained current behavior ANN. Moreover, the root-mean-square error (RMSE) and mean absolute percentage error (MAPE) are calculated after min–max normalization to address value spanning. In this case, the normalized RMSE and MAPE are 0.0152 and 4.79%, respectively.

B. NSGA-III-Based Optimization for c_1 and c_2

Once the ANN-based current behavior structure is trained, incorporating with the predefined physical model of power oscillation, the HPD objective functions are set. The optimization algorithm shown in Fig. 5 is then implemented in MATLAB, with the parameters listed in Table III. In accordance with the parameter range recommended by the authors of NSGA-III [38], 200 generations are used for the four-objective optimization problem to ensure convergence, and the population size is set to 80, which encourages diverse exploration while maintaining computational efficiency. The crossover rate is set to 0.7, indicating that 70% of the population undergoes crossover in each generation, which promotes diversity while balancing exploitation and exploration. The mutation rate, representing the probability of randomly altering the solution of an individual, is defined as 0.5. This ensures substantial exploration of the search space, allowing the algorithm to avoid local optima while maintaining diversity in the population. A step size of 0.001 facilitates precise adjustments in the decision variables, significantly finer than the discretization step of 0.025 used for ANN training, enhancing the data resolution. After all iterations, the population of the final iteration serves as a set of N optimal solutions, from which the optimized CRGs are subsequently determined.

Moreover, Fig. 8 presents a comparative convergence analysis showing that although NSGA-II and NSGA-III algorithms eventually converge to acceptable solution sets, NSGA-III achieves a lower inverted generational distance (IGD) and higher hypervolume (HV) within fewer iterations. This proves a better convergence rate and more uniform distribution across the Pareto front, particularly evident in many-objective settings with four or more objectives. Finally, according to the IEEE Std 519-2022 [48], the upper limit for THD is set at 5% with the current imbalance maintained below 1%, and keeping the power ripple under 15%. By applying these criteria to Algorithm 1, the optimal solutions for c_1 and c_2 considering each objective are identified and presented in Table IV. Notably, the optimal values for ORA and ORR are found simultaneously, resulting in a combined CRGs referred to as ORAR.

VII. Experimental Validation

The experimental results are designed to demonstrate the LVRT capability under traditional, C-IARC, and optimized CRGs determined by the proposed MaO-OCRGS in various

TABLE IV
DECISION VARIABLES FOR THE OPTIMIZED CRGS

CRG	OTHD	OUI	ORAR
Objective	min THD	min UI	min Δp & Δq
c_1	0.1241	0.1306	0.5014
c_2	0.1594	0.1197	0.5236

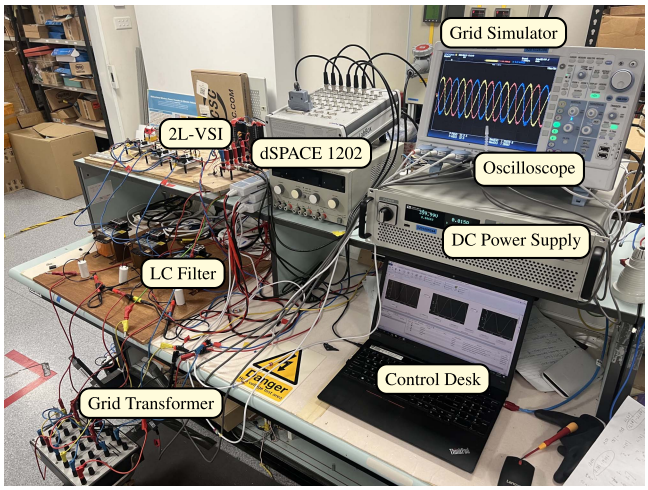

Fig. 9. Experimental setup of the three-phase grid-connected DG system with controller.

sag scenarios. A three-phase grid-connected DG system was built in the laboratory, as illustrated in Fig. 9. The parameters for this setup are detailed in Table III. The CRGs are tested under different sag types (Type B and Type E as defined in IEEE P1668 [49]), as well as different sag depths of 30%, 20%, and 11%. Within each specific sag case, all CRGs are evaluated under identical experimental conditions. Note that, the performance metrics (Δp, Δq, THD, and UI) are quantitatively evaluated through (18)–(20) according to the experimental measurements.

A. *Type B Sag (30% Single-Phase Voltage Dip in Phase a)*

A first set of results showing experimental results of the five traditional CRGs under the Type B sag is presented in Fig. 10. Following the sag detection at $t = 0$ s, a delay of 0.04s is intentionally introduced to show that a minimum of 0.7 p.u. can be reached without a proper LVRT strategy. Then, the five traditional CRGs are sequentially applied during 0.04 s, i.e., two fundamental periods, by simply adjusting the decision variables shown in Table II. In Fig. 10(a) the grid voltage sag in phase a is noticeable, while phase b and phase c remain intact. The corresponding current waveform, instantaneous active power, and reactive power during the different CRGs are presented in Fig. 10(b), (c), and (d), respectively. During the IARC period, a neglectable ripple in power is observed. However, the three-phase current is distorted with the highest THD listed in Table V. In contrast, AARC decreases the THD to the greatest extent at the expense of a pronounced current imbalance. While the BPSC

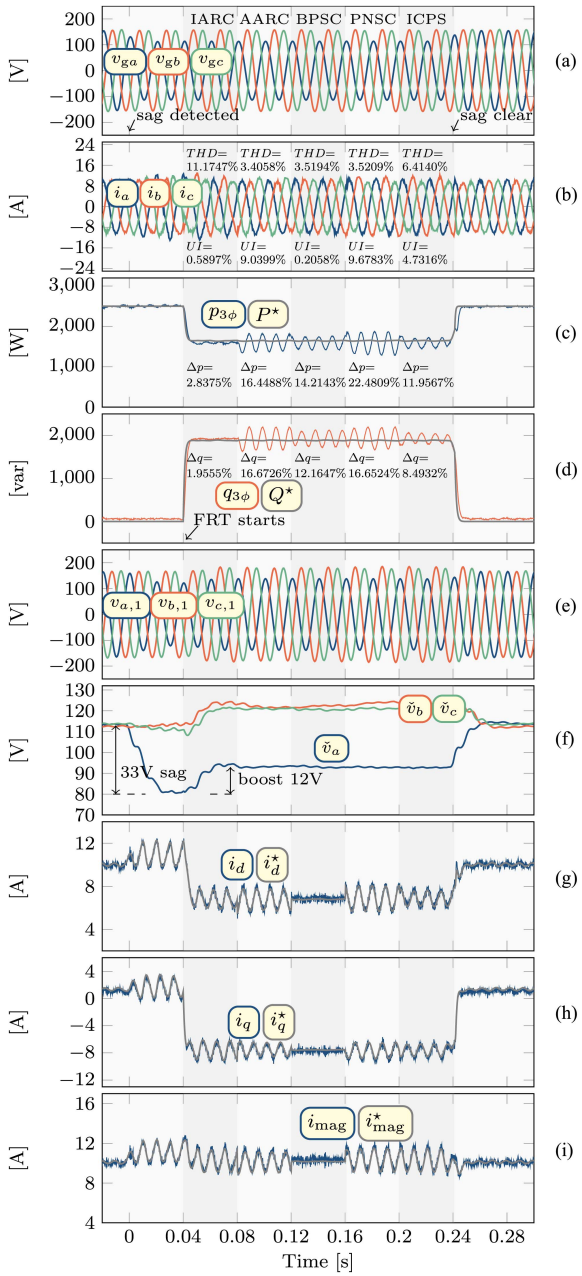

Fig. 10. Experimental results employing the traditional CRGs during Type B sag, IARC (0.04∼0.08 s), AARC (0.08∼ 0.12 s), BPSC (0.12∼ 0.16 s), PNSC (0.16∼ 0.20 s), ICPS (0.20∼ 0.24 s): (a) three-phase grid voltage, (b) three-phase injected current, (c) instantaneous active power and its reference, (d) instantaneous reactive power and its reference, (e) three-phase PCC fundamental voltage, (f) three-phase rms value of PCC voltage, (g) d-axis component of current and its reference, (h) q-axis component of current and its reference, and (i) magnitude of the dq-current and its reference.

CRG nearly eliminates imbalance, both AARC and BPSC enhance current quality, albeit with a more noticeable power ripple. The PNSC CRG demonstrates limited effectiveness when neither the active nor reactive power reference is zero. Although the ICPS CRG aims to address both power and current performance metrics, its results are less than satisfactory. The performance metrics for each CRG are summarized in Table V. These results suggest that the traditional CRGs lack control and flexibility,

TABLE V
EXPERIMENTAL PERFORMANCE METRICS OF THE TRADITIONAL CRGS FOR DIFFERENT SAG TYPES

	CRGs	$THD(\%)$	$UI(\%)$	$\Delta p(\%)$	$\Delta q(\%)$
Type B	IARC	11.1747	0.5897	2.8375	1.9555
	AARC	3.4058	9.0399	16.4488	16.6726
	BPSC	3.5194	0.2058	14.2143	12.1647
	PNSC	3.5209	9.6783	22.4809	16.6524
	ICPS	6.4140	4.7316	11.9567	8.4932
Type E	IARC	10.2557	1.015	2.8011	2.0405
	AARC	3.5267	9.4272	18.1072	18.1941
	BPSC	3.7267	0.2889	15.1016	13.4108
	PNSC	3.7009	9.5715	24.0741	17.8253
	ICPS	6.6572	4.7661	13.1428	9.4184

TABLE VI
EXPERIMENTAL PERFORMANCE METRICS OF THE C-IARC CRGS FOR DIFFERENT SAG TYPES

	k	$THD(\%)$	$UI(\%)$	$\Delta p(\%)$	$\Delta q(\%)$
Type B	0.8	9.3661	1.8442	5.2781	3.9202
	0.6	7.5298	3.7257	8.3621	7.9562
	0.4	5.9494	5.3151	11.7029	11.4283
	0.2	4.1050	7.1745	13.8037	13.8499
Type E	0.8	8.9762	2.0682	4.9825	4.0508
	0.6	7.6318	3.6874	8.2006	7.9088
	0.4	5.8367	5.4536	12.2468	12.0976
	0.2	4.2106	7.0115	15.2939	15.0170

resulting in significant deviations in performance metrics. For instance, the THD from IARC (11.1747%) and the UI from AARC (9.0399%) surpass the predefined thresholds of 5% and 1%, respectively. Furthermore, Fig. 10(e) and (f) shows the PCC voltage, showcasing both the fundamental component and the calculated rms value, respectively. Following the 33 V sag, the PCC voltage is supported by a 12 V boost through the reactive compensation, validating the compensation effectiveness.

A second set of results is obtained for the C-IARC CRG proposed in [28] using the same procedure as the first set. This reflects the transition from IARC to AARC as the parameter k decreases from 1 to 0 in 0.2 steps. Thus, k is used to adjust the tradeoff between power oscillation and current distortion. For the sake of brevity, the results are summarized in Table VI. The power oscillations (Δp and Δq) become more pronounced while the THD is progressively reduced, following the transition from IARC to AARC. Note that the cases of $k = 1$ (IARC) and $k = 0$ (AARC) are excluded from the table to avoid redundancy, as their performance has been reported separately.

A third set of results for the optimized CRGs, i.e., OTHD, OUI, and ORAR, is presented in Fig. 11. By adapting the decision variables according to Table IV, the optimized CRGs are evaluated under the same conditions previously discussed. The performance results of these CRGs are summarized in Table VII. These results are compared with the traditional CRGs and C-IARC CRGs [28]. As a result, a graphical comparison is shown in Fig. 12. As previously mentioned and experimentally

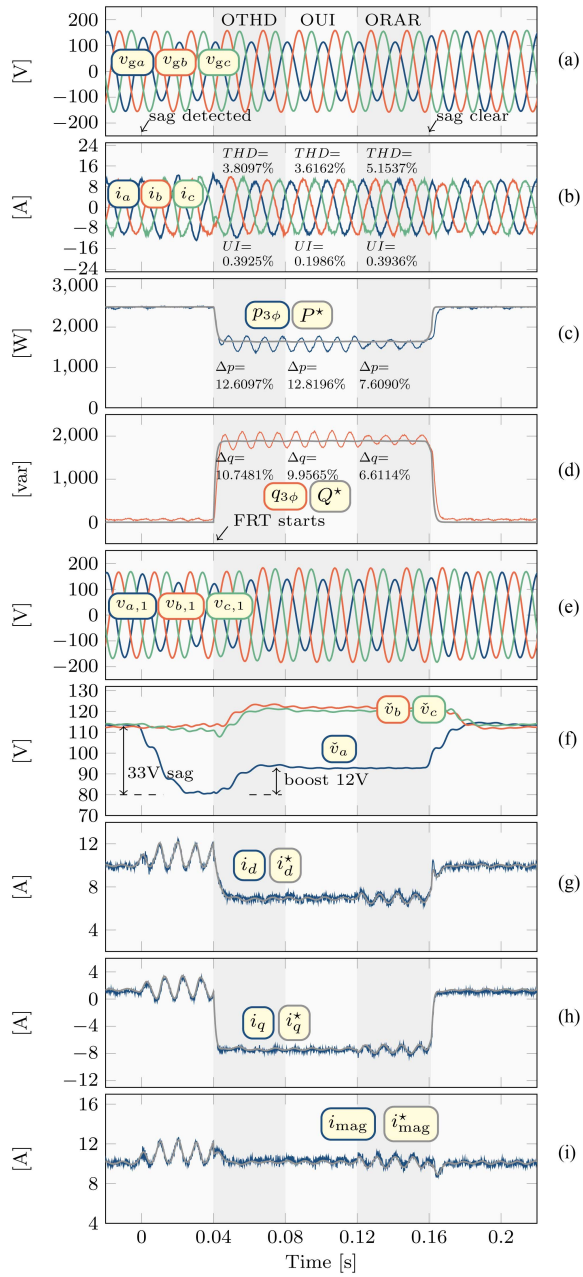

Fig. 11. Experimental results employing the proposed optimized CRGs during Type B sag, OTHD (0.04∼ 0.08 s), OUI (0.08∼ 0.12 s), ORAR (0.12∼ 0.16 s): (a) three-phase grid voltage, (b) three-phase injected current, (c) instantaneous active power and its reference, (d) instantaneous reactive power and its reference, (e) three-phase PCC voltage, and (f) three-phase rms value of PCC voltage, (g) d-axis component of current and its reference, (h) q-axis component of current and its reference, and (i) magnitude of the dq-current and its reference.

validated, AARC minimizes the THD. Therefore, as illustrated in Fig. 12(a), OTHD is compared with AARC. Besides, since the C-IARC cases with $k = 0.2$ and $k = 0.4$ are relatively closer to AARC by design, they are also included in the same figure to facilitate direct comparison. Note that OTHD outperforms AARC in UI, Δp, and Δq, keeping these metrics within the required range, while significantly reducing UI from 9.0399% to 0.3925% along with the decreases of 23.3% and 35.5% in Δp and Δq, respectively, despite a minor tradeoff of an 11.8%

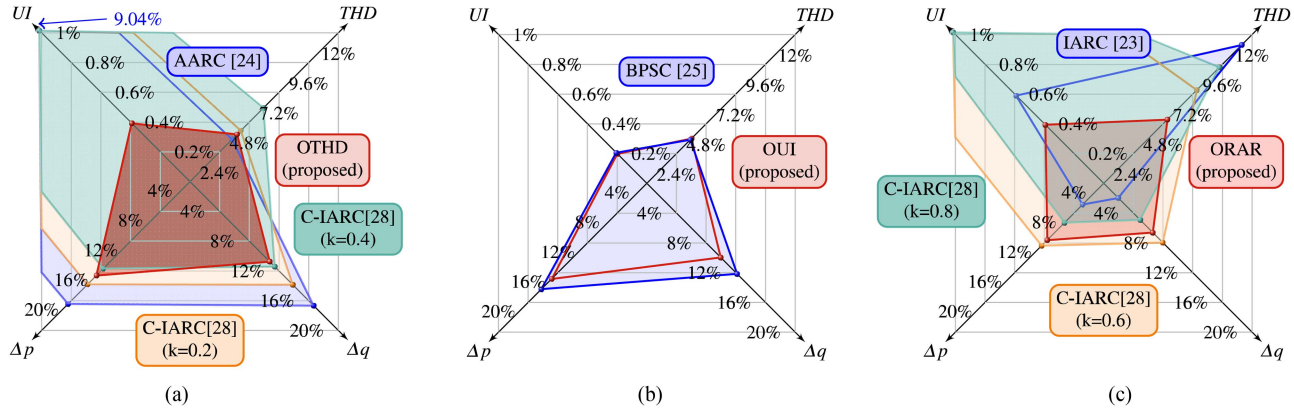

Fig. 12. Overall performance comparison of the optimized CRGs, C-IARC CRGs, and the traditional CRGs during Type B sag in terms of improving: (a) THD, (b) UI, and (c) power ripple (Δp and Δq).

TABLE VII
EXPERIMENTAL PERFORMANCE METRICS OF THE OPTIMIZED CRGS DURING DIFFERENT SAG TYPES

	CRGs	$THD(\%)$	$UI(\%)$	$\Delta p(\%)$	$\Delta q(\%)$
Type B	OTHD	3.8097	0.3925	12.6097	10.7481
	OUI	3.6162	0.1986	12.8196	9.9565
	ORAR	5.1537	0.3936	7.6090	6.6114
Type E	OTHD	3.5449	0.7174	14.4046	12.2717
	OUI	3.5895	0.3184	14.0362	12.2906
	ORAR	5.4333	0.7242	7.8901	7.0328

increase in THD. Although the C-IARC with $k = 0.4$ and $k = 0.2$ achieves a compromise between power oscillation suppression and current distortion by offering flexibility, it does not address current unbalance. Notably, the OTHD exhibits superior performance across all evaluated performance metrics compared to C-IARC with $k = 0.2$, thereby highlighting the multiobjective optimization nature of the proposed MaO-OCRGS. The improvement of OUI over BPSC is also considerable, with the active power ripple reduced by 9.8% and the reactive power ripple lowered by 18.1%, as observed in Fig. 12(b). Similarly, Fig. 12(c) demonstrates that ORAR effectively mitigates the THD over-range by 53.9% associated with IARC and outperforms the C-IARC ($k = 0.6$) in all the performance metrics. While the power-related performance metrics of ORAR may not match that of IARC and C-IARC with $k = 0.8$, the values of Δp and Δq remain within predefined limits. In contrast, the THD and UI of C-IARC under both k values exceed their permissible threshold.

In addition to the steady-state performance metrics discussed above, the transient behavior was also studied. For the sake of brevity, Figs. 10 and 11 show a transient process for IARC and OTHD, respectively. This test was also performed individually, and for all strategies, the nominal current amplitude was around 10 A, and the peak values of both the measured and reference currents remained below 15 A, complying with the 1.5 p.u. limit specified in IEEE 1547-2018 of the latest version [50]. The tracking error was also kept within 10%, indicating the absence of overshoot or excessive current. Moreover, both active and reactive power reached 90% of their steady-state reference values within 10 ms during both FRT initiation and sag recovery, demonstrating a fast transition that complies with, and even outperforms, the timing requirements specified in IEEE 1547-2018.

B. Type E Sag (30% Two-Phase Voltage Dip in Phase b and Phase c)

In another scenario, where a Type E sag is conducted, a new set of optimized CRGs are determined following the same procedure of MaO-OCRGS. The performance metrics for the traditional, C-IARC and the optimized CRGs are listed in Tables V, VI, and VII, respectively, with a comparison illustrated in Fig. 13. Similar to the Type B scenario, the optimized CRGs determined by the proposed MaO-OCRGS significantly optimizes the performance metrics, further restricting their values to remain within predefined limits. Compared to the observation in the Type B scenario, the performance metrics in the Type E scenario are reduced to an even greater extent. An evident example of this is shown in Fig. 13(c), where, with ORAR, both THD and UI are significantly reduced simultaneously, with THD decreasing by 47% and UI by 45%. Moreover, the optimized CRGs provide overall performance enhancements relative to the C-IARC CRGs with $k = 0.2$ and $k = 0.6$ and address the over-limit issue of THD and UI witnessed in the C-IARC results. These results from the Type E scenario, combined with the previously presented Type B results, confirm the superiority of the optimized CRGs across various voltage sag types, i.e., single-phase and two-phase sag.

C. Different Sag Depths

To demonstrate the adaptability of the optimized CRGs, experiments under sag depths of 20% and 11% (single-phase) are conducted and analyzed alongside the 30% Type B case, i.e., a 30% single-phase sag. As shown in Tables VIII–X, the optimized CRGs consistently regulate performance metrics within predefined limits, whereas the traditional CRGs often exceed them. For instance, in 20% and 11% sags, THD with IARC

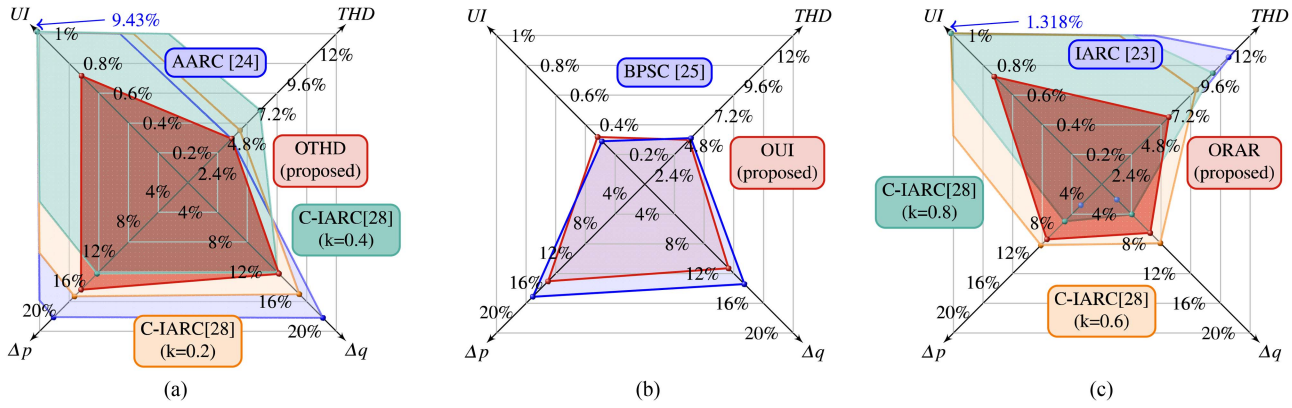

Fig. 13. Overall performance comparison of the optimized CRGs, C-IARC CRGs, and the traditional CRGs during Type E sag in terms of improving: (a) THD, (b) UI, and (c) power ripple (Δp and Δq).

TABLE VIII
EXPERIMENTAL PERFORMANCE METRICS OF THE TRADITIONAL CRGS DURING DIFFERENT SAG DEPTHS

Depth	CRGs	$THD(\%)$	$UI(\%)$	$\Delta p(\%)$	$\Delta q(\%)$
Type B (30%)	IARC	11.1747	0.5897	2.8375	1.9555
	AARC	3.4058	9.0399	16.4488	16.6726
	BPSC	3.5194	0.2058	14.2143	12.1647
	PNSC	3.5209	9.6783	22.4809	16.6524
	ICPS	6.4140	4.7316	11.9567	8.4932
20%	IARC	7.8633	0.3192	1.8938	2.5814
	AARC	2.8617	6.2248	11.3528	11.1521
	BPSC	3.3628	0.1155	8.3962	8.5769
	PNSC	4.3933	6.9769	11.1561	12.9279
	ICPS	5.5833	3.009	6.0883	7.0706
11%	IARC	5.4196	0.2630	2.1279	1.6761
	AARC	2.2327	4.3230	7.6820	8.2728
	BPSC	2.6868	0.0904	5.6269	6.9182
	PNSC	3.9684	3.8205	7.3767	8.3568
	ICPS	5.0497	1.7983	4.253	6.5281

TABLE IX
EXPERIMENTAL PERFORMANCE METRICS OF THE C-IARC CRGS FOR DIFFERENT SAG DEPTHS

Depth	k	$THD(\%)$	$UI(\%)$	$\Delta p(\%)$	$\Delta q(\%)$
Type B (30%)	0.8	9.3661	1.8442	5.2781	4.9202
	0.6	7.5298	3.7257	8.3621	7.9562
	0.4	5.9494	5.3151	11.7029	11.4283
	0.2	4.1050	7.1745	13.8037	13.8499
20%	0.8	6.3057	1.4654	3.9737	3.3190
	0.6	5.2448	2.3842	5.5728	5.6056
	0.4	4.0388	3.4496	7.4477	7.5967
	0.2	3.2976	4.3646	9.8353	10.1721
11%	0.8	3.8131	0.8775	2.3622	2.1238
	0.6	3.6864	1.5066	3.5768	3.3908
	0.4	3.0330	2.2600	4.8563	4.4775
	0.2	2.6276	3.1256	5.7523	5.5766

TABLE X
EXPERIMENTAL PERFORMANCE METRICS OF THE OPTIMIZED CRGS DURING DIFFERENT SAG DEPTHS

Depth	CRGs	$THD(\%)$	$UI(\%)$	$\Delta p(\%)$	$\Delta q(\%)$
Type B (30%)	OTHD	3.8097	0.3925	12.6097	10.7481
	OUI	3.6162	0.1986	12.8196	9.9565
	ORAR	5.1537	0.3936	7.6090	6.6114
20%	OTHD	3.0842	0.2713	6.8041	7.7718
	OUI	3.7567	0.1345	7.1138	7.2003
	ORAR	3.8183	0.1762	4.1376	5.0772
11%	OTHD	2.5327	0.1944	4.2943	5.0756
	OUI	2.5869	0.1124	4.4982	5.5456
	ORAR	3.0005	0.1462	2.4959	3.9440

exceeds the limit of 5% (7.8633% and 5.4196%, respectively) but is reduced by 51.4% and 44.6%, to 3.8183% and 3.0005% with ORAR. Compared to the C-IARC CRGs, the optimized CRGs not only ensure that all performance metrics remain within predefined bounds, including resolving the common over-limit issue of UI, but also deliver overall performance enhancements. For example, under the 20% sag, the OTHD outperforms C-IARC with both $k = 0.4$ and 0.2 across all the performance metric. Similarly, ORAR surpasses C-IARC with $k = 0.6$ and addresses the over-limit of THD (6.3057%) observed in C-IARC with $k = 0.8$.

Note that as sag depth increases, the difference in the performance metrics among optimized CRGs becomes more pronounced. This is expected, as greater voltage imbalance amplifies negative sequence components, making the CRG more sensitive to the introduced decision variables and leading to more substantial, targeted improvements. These results validate the adaptability of the optimized CRGs to ride-through sags with different depths.

Based on the above comparison across various sag types and depths, it can be observed that traditional CRGs typically focus on a single performance metric without explicitly addressing the tradeoffs among multiple conflicting objectives. The C-IARC method provides limited flexibility to adjust the tradeoffs and it

lacks a structured approach for selecting the most appropriate CRG. As a result, some performance metrics may still exceed the required bounds. In contrast, the proposed MaO-OCRGS enables informed selection by optimizing the tradeoffs, identifying optimal CRGs that enhance a desired performance metric while maintaining the others within predefined limits.

VIII. Conclusion

This article presented an MaO-OCRGS suitable for standard LVRT control schemes for DG systems under unbalanced voltage sags. By introducing two decision variables, the proposed strategy integrates the benefits of the traditional CRGs while overcoming their limitations through the simultaneous optimization of four performance metrics: Δp, Δq, THD, and UI. To achieve this, a theoretical framework for power oscillations was derived, and an ANN-based model was developed to analyze current behavior, proposing HPD objective functions. This approach led to the formulation of an MaOO problem, which was addressed based on the NSGA-III algorithm and a postoptimization selection to identify the optimal decision variables and generate the corresponding optimized CRGs. The experimental results show enhanced overall performance compared to traditional and C-IARC CRGs, demonstrating the adaptiveness and effectiveness of the proposed MaO-OCRGS in riding through different sag scenarios, including various sag types and depths. This confirms its potential to improve the operation of DG systems under LVRT conditions. Unlike the traditional ones, the optimized CRGs optimize the performance metrics and maintain them within acceptable limits, therefore offering a more flexible alternative for the operation of DGs during unbalanced voltage sags. Finally, since the influence of grid voltage harmonics and nonideal grid impedance was considered beyond the scope of this work, further research is needed to evaluate their impact on CRG performance under unbalanced conditions.

Acknowledgment

The authors would like to thank Dr. X. Niu from the IAS Lab at Shanghai University of Electric Power for providing the 800V/40A SiC half-bridge power driver boards used in this experiment.

References

[1] N. Anglani and G. Petrecca, "Fossil fuel and biomass fed distributed generation and utility plants: Analysis of energy and environmental performance indicators," in *Proc. 2nd IEEE Int. Symp. Power Electron. Distrib. Gener. Syst.*, 2010, pp. 964–969.

[2] S. Ganguly and D. Samajpati, "Distributed generation allocation on radial distribution networks under uncertainties of load and generation using genetic algorithm," *IEEE Trans. Sustain. Energy*, vol. 6, no. 3, pp. 688–697, Jul. 2015.

[3] F. Yang, Q. Sun, Q.-L. Han, and Z. Wu, "Cooperative model predictive control for distributed photovoltaic power generation systems," *IEEE Trans. Emerg. Sel. Topics Power Electron.*, vol. 4, no. 2, pp. 414–420, Jun. 2016.

[4] K. Macken, K. Vanthournout, J. Van den Keybus, G. Deconinck, and R. Belmans, "Distributed control of renewable generation units with integrated active filter," *IEEE Trans. Power Electron.*, vol. 19, no. 5, pp. 1353–1360, Sep. 2004.

[5] F. Blaabjerg, R. Teodorescu, M. Liserre, and A. Timbus, "Overview of control and grid synchronization for distributed power generation systems," *IEEE Trans. Ind. Electron.*, vol. 53, no. 5, pp. 1398–1409, Oct. 2006.

[6] M. H. Bollen, *Appendix B: IEEE Standards on Power Quality*. New York, NY, USA: IEEE Press, 2000, pp. 481–483.

[7] W. Liu, F. Blaabjerg, D. Zhou, and S.-F. Chou, "Modified instantaneous power control with phase compensation and current-limited function under unbalanced grid faults," *IEEE Trans. Emerg. Sel. Topics Power Electron.*, vol. 9, no. 3, pp. 2896–2906, Jun. 2021.

[8] J. L. Sosa, M. Castilla, J. Miret, J. Matas, and Y. A. Al-Turki, "Control strategy to maximize the power capability of PV three-phase inverters during voltage sags," *IEEE Trans. Power Electron.*, vol. 31, no. 4, pp. 3314–3323, Apr. 2016.

[9] A. Micallef, M. Apap, C. Spiteri-Staines, and J. M. Guerrero, "Single-phase microgrid with seamless transition capabilities between modes of operation," *IEEE Trans. Smart Grid*, vol. 6, no. 6, pp. 2736–2745, Nov. 2015.

[10] L. Labib, A. Merabet, and A. M. Ghias, "Low-voltage ride-through operation of permanent magnet synchronous generator with active and reactive power injection," in *Proc. 44th Annu. Conf. IEEE Ind. Electron. Soc.*, 2018, pp. 1848–1853.

[11] J. Miret, A. Camacho, M. Castilla, L. G. de Vicuna, and J. Matas, "Control scheme with voltage support capability for distributed generation inverters under voltage sags," *IEEE Trans. Power Electron.*, vol. 28, no. 11, pp. 5252–5262, Nov. 2013.

[12] D. I. Brandao, F. E. G. Mendes, R. V. Ferreira, S. M. Silva, and I. A. Pires, "Active and reactive power injection strategies for three-phase four-wire inverters during symmetrical/asymmetrical voltage sags," *IEEE Trans. Ind. Appl.*, vol. 55, no. 3, pp. 2347–2355, May/Jun. 2019.

[13] W. Choi, W. Lee, and B. Sarlioglu, "Reactive power compensation of grid-connected inverter in vehicle-to-grid application to mitigate balanced grid voltage sag," in *Proc. IEEE Power Energy Soc. Gen. Meeting*, 2016, pp. 1–5.

[14] A. Timbus, M. Liserre, R. Teodorescu, P. Rodriguez, and F. Blaabjerg, "Evaluation of current controllers for distributed power generation systems," *IEEE Trans. Power Electron.*, vol. 24, no. 3, pp. 654–664, Mar. 2009.

[15] D. Shin, K.-J. Lee, J.-P. Lee, D.-W. Yoo, and H.-J. Kim, "Implementation of fault ride-through techniques of grid-connected inverter for distributed energy resources with adaptive low-pass notch PLL," *IEEE Trans. Power Electron.*, vol. 30, no. 5, pp. 2859–2871, May 2015.

[16] S. Alepuz et al., "Control strategies based on symmetrical components for grid-connected converters under voltage dips," *IEEE Trans. Ind. Electron.*, vol. 56, no. 6, pp. 2162–2173, Jun. 2009.

[17] L. Liu, H. Li, Y. Xue, and W. Liu, "Reactive power compensation and optimization strategy for grid-interactive cascaded photovoltaic systems," *IEEE Trans. Power Electron.*, vol. 30, no. 1, pp. 188–202, Jan. 2015.

[18] M. R. K. Rachi, M. A. Awal, and I. Husain, "Asymmetrical fault ride-through and power oscillation characterization for grid-tied voltage source converters," *IEEE Trans. Ind. Appl.*, vol. 59, no. 4, pp. 4550–4561, Jul./Aug. 2023.

[19] R. M. Silva, A. F. Cupertino, G. M. Rezende, C. V. Sousa, and V. F. Mendes, "Power control strategies for grid connected converters applied to full-scale wind energy conversion systems during LVRT operation," *Electr. Power Syst. Res.*, vol. 184, 2020, Art. no. 106279.

[20] R. K. Varma and H. Maleki, "PV solar system control as STATCOM (PV-STATCOM) for power oscillation damping," *IEEE Trans. Sustain. Energy*, vol. 10, no. 4, pp. 1793–1803, Oct. 2019.

[21] Z. Zhang et al., "Negative sequence current regulation based power control strategy for vienna rectifier under unbalanced grid voltage dips," *IEEE Trans. Ind. Electron.*, vol. 71, no. 2, pp. 1170–1180, Feb. 2024.

[22] X. Niu, C. Zhang, Y. Qu, X. Wang, and H. Li, "A new composite control strategy for large-signal stabilization of constant power loads in islanded AC microgrids," *IEEE Trans. Smart Grid*, vol. 15, no. 5, pp. 4407–4423, Sep. 2024.

[23] P. Rodriguez, A. V. Timbus, R. Teodorescu, M. Liserre, and F. Blaabjerg, "Flexible active power control of distributed power generation systems during grid faults," *IEEE Trans. Ind. Electron.*, vol. 54, no. 5, pp. 2583–2592, Oct. 2007.

[24] N. F. Ibrahim, K. Mahmoud, M. Lehtonen, and M. M. F. Darwish, "Comparative analysis of three-phase PV grid connected inverter current control schemes in unbalanced grid conditions," *IEEE Access*, vol. 11, pp. 42204–42221, 2023.

[25] J. Jia, G. Yang, and A. H. Nielsen, "A review on grid-connected converter control for short-circuit power provision under grid unbalanced faults," *IEEE Trans. Power Del.*, vol. 33, no. 2, pp. 649–661, Apr. 2018.
[26] A. A. Montanari and A. M. Gole, "Enhanced instantaneous power theory for control of grid connected voltage sourced converters under unbalanced conditions," *IEEE Trans. Power Electron.*, vol. 32, no. 8, pp. 6652–6660, Aug. 2017.
[27] S. F. Zarei, H. Mokhtari, M. A. Ghasemi, S. Peyghami, P. Davari, and F. Blaabjerg, "Control of grid-following inverters under unbalanced grid conditions," *IEEE Trans. Energy Convers.*, vol. 35, no. 1, pp. 184–192, Mar. 2020.
[28] S. Pola, M. Azzouz, A. S. A. Awad, and H. Sindi, "Fault ride-through strategies for synchronverter-interfaced energy resources under asymmetrical grid faults," *IEEE Trans. Sustain. Energy*, vol. 14, no. 4, pp. 2391–2405, Oct. 2023.
[29] A. Camacho, M. Castilla, J. Miret, J. C. Vasquez, and E. Alarcon-Gallo, "Flexible voltage support control for three-phase distributed generation inverters under grid fault," *IEEE Trans. Ind. Electron.*, vol. 60, no. 4, pp. 1429–1441, Apr. 2013.
[30] M. A. Garnica Lopez, J. L. Garcia de Vicuna, J. Miret, M. Castilla, and R. Guzman, "Control strategy for grid-connected three-phase inverters during voltage sags to meet grid codes and to maximize power delivery capability," *IEEE Trans. Power Electron.*, vol. 33, no. 11, pp. 9360–9374, Nov. 2018.
[31] M. Castilla, J. Miret, J. L. Sosa, J. Matas, and L. G. D. Vicuna, "Grid-fault control scheme for three-phase photovoltaic inverters with adjustable power quality characteristics," *IEEE Trans. Power Electron.*, vol. 25, no. 12, pp. 2930–2940, Dec. 2010.
[32] F. Wen, P. Acuna, J. Yang, Z. Yuan, and A. M. Y. M. Ghias, "Low-voltage ride-through scheme for distributed generation inverters using a modified current reference strategy," in *Proc. IEEE Int. Conf. Ind. Technol.*, 2024, pp. 1–7.
[33] J. Lamb and B. Mirafzal, "Active and reactive power operational region for grid-interactive cascaded h-bridge multilevel converters," in *Proc. IEEE 7th Int. Symp. Power Electron. Distrib. Gener. Syst.*, 2016, pp. 1–6.
[34] R. Wang, F. Xie, B. Zhang, Y. Chen, and D. Qiu, "Hybrid data-mechanism modeling for power loss of a boost converter," *IEEE Trans. Emerg. Sel. Topics Power Electron.*, vol. 11, no. 6, pp. 5582–5591, Dec. 2023.
[35] A. Bhattacharya and C. Chakraborty, "A shunt active power filter with enhanced performance using ann-based predictive and adaptive controllers," *IEEE Trans. Ind. Electron.*, vol. 58, no. 2, pp. 421–428, Feb. 2011.
[36] X. Shen, Y. Zuo, J. Kong, and W. Martinez, "Artificial intelligence applications in high-frequency magnetic components design for power electronics systems: An overview," *IEEE Trans. Power Electron.*, vol. 39, no. 7, pp. 8478–8496, Jul. 2024.
[37] T. Dragičević and M. Novak, "Weighting factor design in model predictive control of power electronic converters: An artificial neural network approach," *IEEE Trans. Ind. Electron.*, vol. 66, no. 11, pp. 8870–8880, Nov. 2019.
[38] K. Deb and H. Jain, "An evolutionary many-objective optimization algorithm using reference-point-based nondominated sorting approach, part I: Solving problems with box constraints," *IEEE Trans. Evol. Comput.*, vol. 18, no. 4, pp. 577–601, Aug. 2014.
[39] Y. Ai, M. Du, Z. Pan, and G. Li, "The optimization of reactive power for distribution network with PV generation based on NSGA-III," *CPSS Tran. Power Electron. Appl.*, vol. 6, no. 3, pp. 193–200, 2021.
[40] K. Ji et al., "High frequency stability constraints based MMC controller design using NSGA-III algorithm," *CSEE J. Power Energy Syst.*, vol. 9, no. 2, pp. 623–633, 2023.
[41] H. Ishibuchi, R. Imada, Y. Setoguchi, and Y. Nojima, "Performance comparison of NSGA-II and NSGA-III on various many-objective test problems," in *Proc. IEEE Congr. Evol. Comput.*, 2016, pp. 3045–3052.
[42] H. Akagi, E. H. Watanabe, and M. Aredes, "The Instantaneous Power Theory," in *Instantaneous Power Theory and Applications to Power Conditioning*. Hoboken, NJ, USA: Wiley, 2007, pp. 41–107.
[43] G. Saccomando and J. Svensson, "Transient operation of grid-connected voltage source converter under unbalanced voltage conditions," in *Proc. 36th Ind. Appl. Conf. Annu. Meeting*, 2001, pp. 2419–2424.
[44] Z. Xin, X. Wang, Z. Qin, M. Lu, P. C. Loh, and F. Blaabjerg, "An improved second-order generalized integrator based quadrature signal generator," *IEEE Trans. Power Electron.*, vol. 31, no. 12, pp. 8068–8073, Dec. 2016.
[45] P. Rodriguez, A. Luna, I. Candela, R. Teodorescu, and F. Blaabjerg, "Grid synchronization of power converters using multiple second order generalized integrators," in *Proc. 34th Annu. Conf. IEEE Ind. Electron.*, 2008, pp. 755–760.
[46] S. Pola, M. Azzouz, A. S. A. Awad, and H. Sindi, "Fault ride-through strategies for synchronverter-interfaced energy resources under asymmetrical grid faults," *IEEE Trans. Sustain. Energy*, vol. 14, no. 4, pp. 2391–2405, Oct. 2023.
[47] K. Man, K. Tang, and S. Kwong, "Genetic algorithms: Concepts and applications [in engineering design]," *IEEE Trans. Ind. Electron.*, vol. 43, no. 5, pp. 519–534, Oct. 1996.
[48] *IEEE Standard for Harmonic Control in Electric Power Systems*, IEEE Standard 519-2022 (Revision of IEEE Std 519-2014), pp. 1–31, 2022.
[49] *IEEE Approved Draft Recommended Practice for Voltage Sag and Short Interruption Ride-Through Testing for End-Use Electrical Equipment Rated Less Than 1000V*, IEEE P1668/D3, Mar. 2017.
[50] *IEEE Application Guide for IEEE Std 1547-2018, IEEE Standard for Interconnection and Interoperability of Distributed Energy Resources With Associated Electric Power Systems Interfaces*, IEEE Standard 1547.2-2023 (Revision of IEEE Std 1547.2-2008), pp. 1–291, 2024.

Fankai Wen (Graduate Student Member, IEEE) received the B.E. degree in electrical engineering from the Shandong University of Science and Technology, Qingdao, China, in 2021, and the M.S. degree in power engineering in 2022 from Nanyang Technological University (NTU), Singapore, where he is currently working toward the Ph.D. degree with the Energy Research Institute @ NTU, under the Interdisciplinary Graduate Programme.

His research interests include dc–ac converters, control of inverters, distributed generation systems, data-driven methods, and application of optimization in power electronics.

Pablo Acuna (Member, IEEE) received the B.Sc. degree, the B.Eng. degree, and the Ph.D. degree from the Universidad de Concepcion, Chile, in 2004, 2007, and 2013, respectively, all in electronics engineering.

He is currently an Associate Professor with the Department of Electrical Engineering, Universidad de Talca, Chile. His research interests include electrical power conversion systems and their applications in industry, transportation, and utility.

Zhige Yuan received the B.S. degree in electrical engineering and automation from the South China University of Technology, Guangzhou, China, in 2022, and the M.Eng. degree in power electronics in 2024 from the School of Electrical and Electronic Engineering, Nanyang Technological University (NTU), Singapore, where he is currently working toward the Ph.D. degree in power electronics.

His research interests include battery energy storage systems and the application of artificial intelligence in power electronics.

Chenggang Cui (Member, IEEE) received the B.E. degree in automation engineering from Jilin University, Changchun, China, in 2004, the Ph.D. degree in control theory and control from Zhejiang University, Hangzhou, China, in 2010.

He worked with the Shanghai Institute for Advanced Studies, Chinese Academy of Sciences, engaged in energy management and optimal scheduling from 2012 to 2015. He has been with the School of Automation, Shanghai University of Electric Power, where he is currently an Associate Professor. His research interests include the control and schedule of renewable energy systems and microgrid.

Ricardo P. Aguilera (Member, IEEE) received the B.Sc. degree in electrical engineering from the Universidad de Antofagasta, Antofagasta, Chile, the M.Sc. degree in electronics engineering from the Universidad Tecnica Federico Santa María, Valparaiso, Chile, and the Ph.D. degree in electrical engineering from The University of Newcastle, Callaghan, NSW, Australia, in 2003, 2007, and 2012, respectively.

Since 2016, he has been with the University of Technology Sydney, Ultimo, NSW, Australia, where he is currently an Associate Professor. His research interests include model predictive control for power electronics, renewable energy integration, and microgrids.

Amer M. Y. M. Ghias (Senior Member, IEEE) received the B.Sc. degree in electrical engineering from Saint Cloud State University, St Cloud, MN, USA, in 2001, the M.Eng. degree in telecommunications from the University of Limerick, Limerick, Ireland, in 2006, and the Ph.D. degree in electrical engineering from the University of New South Wales (UNSW), Sydney, Australia, in 2014.

He has over seven years of industry experience in Kuwait as an Electrical Engineer, Project Engineer, and Project Manager, before transitioning to academia with appointments with UNSW Australia and the University of Sharjah, UAE. He is currently an Assistant Professor with the School of Electrical and Electronic Engineering, Nanyang Technological University (NTU), Singapore, and serves as the Cluster Director of Power Electronics, Energy Research Institute @ NTU (ERI@N). His research interests include advanced power electronics, hybrid energy storage, model predictive control, smart grids, cable diagnostics, cyber-physical security of power systems, and next-generation multilevel converter technologies.

Dr. Ghias is an Associate Editor of *IET Power Electronics*. He has delivered invited keynote presentations, including at the Rohde & Schwarz Technology Symposium and special sessions and tutorials at the IEEE IAS Annual Meetings in 2024 (Phoenix, USA) and 2025 (New Taipei, Taiwan).